



Title	Dynamical downscaling of future sea-level change in the western North Pacific using ROMS
Author(s)	劉, 昭君
Citation	北海道大学. 博士(理学) 甲第12241号
Issue Date	2016-03-24
DOI	10.14943/doctoral.k12241
Doc URL	http://hdl.handle.net/2115/61708
Type	theses (doctoral)
File Information	Zhaojun_Liu.pdf



[Instructions for use](#)

Dynamical downscaling of future sea-level change
in the western North Pacific using ROMS

(ROMS を用いた力学的ダウンスケーリングによる
北西太平洋の将来海面高度変化の予測)

Thesis for a Doctorate

Zhao-Jun Liu

劉 昭君

Department of Natural History Sciences, Graduate School of Science,
Hokkaido University, Sapporo, 060-0810, Japan

北海道大学大学院理学院自然史科学専攻

March, 2016

Abstract

The future regional sea-level (RSL) rise in the western North Pacific is investigated by dynamical downscaling with the Regional Ocean Modeling System (ROMS) with an eddy-permitting 0.25° resolution based on three Coupled Model Intercomparison Project Phase 5 (CMIP5) climate models—MIROC-ESM, CSIRO-Mk3.6.0, and GFDL-CM3—under the highest greenhouse-gas emission Representative Concentration Pathway (RCP) 8.5 scenario. The dynamical downscaling is performed for two epochs, historical run (1950–2000) and future run (2051–2100). The historical run, ROMS-Hist, is forced with the air-sea fluxes calculated from Coordinated Ocean Reference Experiment version 2 (COREv2). Three future runs—ROMS-MIROC, ROMS-CSIRO, and ROMS-GFDL—are forced with an atmospheric field constructed by adding the difference between the climate model parameters for the 21st and 20th century to the forcing fields in ROMS-Hist.

The downscaled future RSLs commonly exhibit strong, bullseye-like RSL rise maxima centered on 41°N , 142°E to the east of the Tsugaru Strait, and three zonally aligned maxima along 37°N between 140°E and 160°E . In all ROMS downscaling, the RSL rise along the eastern coast of Japan is generally one-third or less of the RSL rise maxima off the eastern coast of Japan. The projected regional (total) sea level rises along Honshu coast during 2081–2100 relative to 1981–2000 are 22–29 (101–108), 8–15 (73–80), and 8–18 (80–90) cm in ROMS-MIROC, ROMS-CSIRO, and ROMS-GFDL, respectively. The largest downscaled RSL rise along the Japan coast occurs at the Sanriku coast in all models. Although the CMIP5 models substantially underestimate the maxima of the offshore RSL rise compared with the ROMS downscaling, the discrepancies of the RSL rise along the Honshu coast between the climate models and ROMS downscaling are less than 10 cm. The maxima of the RSL rise to the east of the Tsugaru Strait and

those along 37°N are probably related to the enhanced northward intrusion of the Kuroshio Current along the eastern coast of Japan and to the northward shift of the Kuroshio Extension, respectively. The projected RSL change along Hokkaido coast during 2081–2100 relative to 1981–2000 is smaller than that on Honshu coast. At Okinawa Island, RSL changes are nearly 30 cm in ROMS-MIROC and ROMS-CSIRO, which is higher than those along Honshu. The difference of RSL rise at Okinawa Island between ROMS-CSIRO and CSIRO-Mk3.6.0 exceeds 10 cm.

ROMS-MIROC and ROMS-GFDL simulations suggest that the RSL changes are likely induced by wind stress changes rather than heat or freshwater fluxes at the surface, whereas ROMS-CSIRO suggests that heat and freshwater fluxes play relatively larger roles than other two models. All ROMS simulations commonly show that the thermosteric components give the major features of regional dynamic height (RDH) and thus major regional sea-level changes, while halosteric components contribute to yield overall meridional gradients in regional sea-level changes.

Table of Contents

Abstract

1. Introduction	5
2. Methods and Data	10
2.1. Global climate models	10
2.2. Regional ocean model	11
2.3. ROMS experiment settings	12
a. Historical run (1951–2000)	13
b. Future run (2051–2100)	13
2.4. Regional sea level	14
2.5. Observational data	15
3. Results	16
3.1. Comparison of ROMS-Hist and observations	16
3.2. Regional sea level changes around Japan	18
3.3. Three-dimensional oceanic changes	22
4. Summary and Discussion	29
Acknowledgements	35
References	36
Figures	44

1. Introduction

Sea level rise due to global warming is one of the most important changes that the ocean will undergo. Global mean sea level has risen at a rate of 3.2 ± 0.4 mm year⁻¹ over 1993–2012 based on satellite altimeter sea surface height (SSH) observations (Cazenave and Cozannet 2014). The recent Intergovernmental Panel on Climate Change (IPCC) Fifth Assessment Report (AR5) indicated that the global mean sea level rise in the 5% to 95% possibility range for the period 2081-2100 compared with 1986-2005 is likely to be 45 to 82 cm for the highest emission scenario Representative Concentration Pathway (RCP) 8.5 (Church et al. 2013).

However, in response to a changing climate, sea level changes are not geographically uniform, but have substantial regionality, as indicated by observational analysis (Bindoff et al. 2007; Cazenave and Cozannet 2014) and coupled climate models (Landerer et al. 2007; Yin et al. 2010; Yin 2012). Based on the satellite records for 1993-2012, the sea level in the western tropical Pacific and eastern Indian Oceans increased much faster than the global mean. In the Atlantic, the sea level rose over the whole basin except for the Gulf Stream region in this period, whereas the sea level fell in the eastern tropical Pacific (Cazenave and Cozannet 2014). Using ensemble projections of 12 models of Coupled Model Intercomparison Project Phase 3 (CMIP3) under the Special Report on Emission Scenario (SRES) A1B, Yin et al. (2010) calculated the dynamic sea level (sea level deviation from the geoid) during 2091-2100 relative to 1981-2000, and found dipole sea level rise patterns in the North Atlantic and North Pacific, and a belt-like pattern in the Southern Ocean. Furthermore, Yin (2012) analyzed 34 models of the Coupled Model Intercomparison Project Phase 5 (CMIP5) and found that there is overall consistency

between the projections of regional sea level (RSL, the deviation of SSH from the global mean value) change by the end of 21st century based on CMIP5 and CMIP3 models for similar scenarios. Various mechanism, such as surface wind changes, and surface heat and freshwater flux changes, can induce the non-uniform dynamic sea level change in response to climate warming. (Sakamoto et al. 2005; Sato et al. 2006; Lowe and Gregory 2006; Landerer et al. 2007; Yin et al. 2010; Suzuki and Ishii 2011a; Sueyoshi and Yasuda 2012; Zhang et al. 2014).

In response to global warming, the future sea level rise in the North Pacific will increase dramatically in the western subtropical gyre east of Japan (Yin et al. 2010; Yin 2012; Sueyoshi and Yasuda 2012). The large sea level rise is related to the changes of Kuroshio Extension (KE), which has a steep meridional sea level gradient, or to larger heat uptake of water masses. Sasaki et al. (2014) recently showed the large sea level variability in the KE region in relation to meridional shifts of the KE jet on decadal timescales, based on tide-gauge and satellite-derived SSH data. Using an atmosphere-ocean coupled climate model, Sakamoto et al. (2005) showed a large sea level rise south of the KE associated with the intensification of the KE in response to global warming. In contrast, Sato et al. (2006) showed a large sea level rise east of Japan associated with a poleward shift of the KE by using a North Pacific ocean general circulation model. Sueyoshi and Yasuda (2012) analyzed 15 CMIP3 models and found that some models exhibit a larger northward shift of the KE, and that others exhibit a greater intensification of the KE. They further suggested that different projected changes in the wind stress caused by changes in atmospheric circulations over the North Pacific result in different responses of the KE, which characterize the different patterns of RSL rise in the western North Pacific. Suzuki and Ishii (2011a) investigated sea level changes caused by CO₂-

induced climate warming by using an atmosphere-ocean coupled climate model. They found that heat flux changes are more important than wind stress changes for RSL rise in the southern recirculation of the KE in their model. Suzuki and Ishii (2011b) decomposed baroclinic sea level changes based on the gridded observational data set into vertical modes, and found that the global warming signals are subducted into the ocean interior. This observation might be related to the formation of the North Pacific subtropical mode water around the KE region and the southern recirculation.

Japan is one of countries most likely to be affected by the sea level rise in the western North Pacific caused by global warming (Hansen et al. 2011). The Organization for Economic Co-operation and Development (OECD) report (Nicholls et al. 2008) evaluated the risk of coastal cities over the world for future coastal flooding, and the Japanese cities Tokyo, Osaka-Kobe, and Nagoya are the 8th, 13th, and 17th cities measured by assets most exposed to coastal flooding in the 2070s, respectively. Therefore, there is a practical need for projections of RSL change caused by climate change along the Japanese coast.

However, the response of the Japanese coastal sea level to ocean circulation changes caused by global warming has not yet been adequately studied. Current climate models may not represent coastal sea level changes properly in the western North Pacific because the model resolutions are too coarse to resolve the narrow western boundary currents and the coastal topographies of islands. The most widely used approach to solve this problem is dynamical downscaling, which has recently been applied to projecting the effects of climate change on oceans (Meier 2006; Sato et al. 2006; Ådlandsvik 2008; Sun et al. 2012; Chamberlain et al. 2012; Liu et al. 2013; Oliver et al. 2014; Seo et al. 2014; Liu et al. 2015). For example, Sato et al. (2006) conducted dynamical downscaling to study global warming-induced changes in North Pacific ocean circulations around Japan by

using a North Pacific ocean general circulation model driven by the sea surface flux derived from MRI-CGCM2.2, which is a climate model contributing to CMIP3. Their model covers the domain 15°S–65°N and 100°E–75°W, with a horizontal resolution of 1/4° (zonally) and 1/6° (meridionally). They reported that coastal sea level rise along Japan is 12–18 cm (including the global mean thermal expansion of 10 cm, but ignoring land-ice melt etc.) from 2000 to 2070, smaller than about 40 cm sea level rise off the east of Japan. However, the spatial distribution of sea level changes along the coasts of Japan was not mentioned by Sato et al. (2006). Moreover, because they did not choose the climate model to be downscaled with a strategy for future sea level rise, it is not clear whether or not their results, obtained from downscaling of only one climate model, are representative. Different climate models produce different sea level changes (e.g., Sueyoshi and Yasuda 2012). Seo et al. (2014) performed dynamical downscaling for the North Pacific marginal seas and thus their regional model covers the area 118°E–155°E and 18°N–50°N, which may be suitable for these marginal seas but not for the western North Pacific to the east of Japan. Therefore, downscaling of future RSL changes in the western North Pacific with an appropriate strategy is required. In this study, we examine future Japanese coastal RSL rise by dynamical downscaling with the Regional Ocean Modeling System (ROMS) based on CMIP5 models outputs. For proper representation of western boundary currents, which result from basin-scale atmospheric forcing, the ROMS domain should cover the whole zonal extent of the North Pacific basin, which is much wider than those in most previous downscaling studies (Meier 2006; Ådlandsvik 2008; Sun et al. 2012; Chamberlain et al. 2012; Liu et al. 2013; Oliver et al. 2014; Seo et al. 2014; Liu et al. 2015). Dynamical downscaling involves a tradeoff between resolution and number of experiments because of the limitation of computational resources.

Therefore, we conduct downscaling of three CMIP5 models, which are selected to investigate the worst-case scenario. That is, we choose the three CMIP5 models that are likely to show the largest RSL rise around Japan to evaluate the upper limits of sea level rise. Detailed procedures of the downscaling and the CMIP5 models used in this study are described in the next section.

The rest of the present paper is organized as follows. In Section 2, the CMIP5 models used for the downscaling are selected, and the main features of the models are introduced. The methods used to generate the initial conditions, lateral boundary conditions, and the atmospheric forcing fields required for the ROMS are described. In Section 3, we compare the downscaled changes and those in the climate model projections and examine the RSL changes around Japan by the end of twenty-first century. The summary and discussion are presented in Section 4.

2. Methods and Data

2.1 Global climate models

The CMIP5 climate model simulations used by the IPCC AR5 are mainly accessed through the Program for Climate Model Diagnosis and Intercomparison (PCMDI, website: <http://cmip-pcmdi.llnl.gov/cmip5/>). To project future climate change associated with increasing concentrations of greenhouse gases, the CMIP5 climate models were integrated under RCP scenarios (Moss et al. 2010). In order to investigate the possible large sea level rise in the western North Pacific, we focus our attention on the highest emission scenario of RCP8.5, and climate models that have highest RSL rise near Japan. This strategy allow us to know the worst-case scenario of RSL rise around Japan. Figure 1a shows the spatially averaged projected RSL change over a domain bounded by 25°N–40°N and 125°E–180°E for the 2081–2100 period relative to the 1981–2000 period for 33 CMIP5 models under the RCP8.5 scenario. RSL is used in this study because we are interested in the regional expression of sea level rise. This domain is used for the average because the region shows significant sea level rise in multi-model ensemble mean from 34 models (Yin 2012). We select the three models with the largest area-averaged RSL rise, which are the MIROC-ESM, the CSIRO-Mk3.6.0, and the GFDL-CM3, as base models for the future dynamical downscaling. The global mean surface air temperature change for 2081–2100 period relative to the 1981–2000 period for 33 CMIP5 models under the RCP8.5 scenario (Fig. 1b) reveals that in the three CMIP5 models, the global mean surface air temperature increase larger compared with most of CMIP5 models. The global thermosteric sea level change is available for 22 CMIP5 models (Fig. 1c). Although it is not available for GFDL-CM3, in MIROC-ESM and CSIRO-Mk3.6.0, the global thermosteric sea level rise large, especially in MIROC-ESM.

The major features of the three CMIP5 models are as follows. In the MIROC-ESM, the ocean component is the Center for Climate System Research (University of Tokyo) Ocean Component model (COCO3.4). The longitudinal grid spacing is about 1.4° , whereas the latitudinal grid intervals gradually vary from 0.5° at the equator to 1.7° near the North/South Poles (Watanabe et al. 2011). In the CSIRO-Mk3.6, the ocean component is the Modular Ocean Model (MOM2.2) with a horizontal resolution of $1.875^\circ \times 0.9375^\circ$ (Rotstayn et al. 2010; Jeffrey et al. 2013). The ocean model component of the GFDL-CM3 uses MOM4p1 code. The ocean model resolution is 1° for longitude. The meridional resolution gradually transitions from $1/3^\circ$ at the equator to 1° at 30°N and remains as 1° between 30°N and 65°N . In the Arctic north of 65°N , a tripolar horizontal grid with poles over Eurasia, North America, and Antarctica is used to eliminate polar filtering over the Arctic (Griffies et al. 2005; Griffies et al. 2011).

2.2 Regional ocean model

The present study uses ROMS to downscale and project sea level changes caused by climate change dynamically. The ROMS can be used for a diverse range of applications from local to planetary scales (e.g., Curchiser et al. 2005; Seo et al. 2007; Ådlandsvik 2008; Lorenzo et al. 2008; Han et al. 2009; Seo et al. 2014). The model solves the incompressible and hydrostatic primitive equations, and uses a free sea surface on horizontally curvilinear coordinates and a generalized terrain-following sigma vertical coordinates (Haidvogel et al. 2000; Shchepetkin and McWilliams. 2005).

We tested several horizontal domains for a reasonable representation of western boundary currents, and found it is necessary to include the whole zonal extent of the basin, when we have only coarse resolution data available in climate models. Thus model

domain covers almost the entire North Pacific basin (110°E–100°W, 5°N–50°N; Fig. 2a). Based on this domain, integration time long-enough for wind-driven gyre spin-up, and computational resource available for us, we decide that the model with an eddy-permitting 0.25°×0.25° horizontal resolution and 32 sigma-levels in the vertical. It is known that eddy permitting model has biases such as the Kuroshio's northward overshooting along eastern coast of Japan (Shu et al. 2013) and northward shift of the KE (Sumata et al. 2012). Therefore, in order to make the future projection with this eddy permitting model more useful, we examine biases in the model compared with observations, as described in Section 3.1, and consider the biases in interpreting the downscaled results.

Schemes used for boundary conditions and mixing are as follows. The clamped lateral boundary condition, in which the boundary value is set to a known exterior value, is used for the barotropic velocities and three dimensional fields, which are temperature, salinity, and zonal and meridional velocities, along the open boundaries at 5°N, 50°N, 110°E, and 100°W. The boundary condition for sea surface elevation is the gradient method in which the outside value is set equal to the closest interior value resulting in a zero-gradient at the edge (Marchesiello et al. 2001). Harmonic horizontal mixing along an epineutral (constant density) surface is applied to the tracers, whereas biharmonic horizontal mixing along constant sigma surfaces is applied to the momentum. A third-order upstream horizontal advection scheme and fourth-order centered vertical advection scheme for momentum and tracer equations are used (Shchepetkin and McWilliams. 2005). K-profile turbulence closure (Large et al. 1994) is used for vertical mixing, and quadratic drag is applied to the bottom friction.

2.3 ROMS experiment settings

a. Historical run (1951-2000)

The historical run (ROMS-Hist) for the period 1951–2000 provides a reference for interpreting future run results. Initial salinity and potential temperature are set as the climatology of the World Ocean Atlas 2009 (WOA2009) (Locarnini et al. 2010; Antonov et al. 2010), and the initial sea level and velocities are set to zero. At the surface, the historical run is forced with six-hourly averaged winds, air temperature, sea level pressure, specific humidity, daily shortwave and downward longwave radiation, and monthly precipitation fields of the Coordinated Ocean Reference Experiment version 2 (CORE v2) (Large and Yeager 2008) from 1951 to 2000. Upward longwave radiation is dependent on sea surface temperature (SST). Surface wind stress and net heat fluxes are computed by using a bulk formula (Fairall et al. 2003). The model sea surface salinity is restored to the climatology values of CORE v2 data with a 30-day period. The lateral boundary values are provided from monthly mean Simple Ocean Data Assimilation version 2.2.4 (SODA2.2.4) in the period from 1951 to 2000 (Carton and Giese 2008).

b. Future run (2051-2100)

Because CMIP5 models have biases in parameters that are used for momentum and heat flux calculations in downscaling in the present climate (Lee et al. 2013), the future run in the late 21st century is forced with atmospheric fields constructed by adding the monthly mean difference between the CMIP5 model parameters from the 21st and 20th century to observed parameters, which are mostly six-hourly, in the 20th century. The details of the approach are as follows. First, we calculated the monthly mean changes for each 100 year interval between 2051–2100 (RCP8.5) and 1951–2000 (CMIP5 historical) in each month and year for the CMIP5 models' simulated winds, air temperature, relative

humidity, sea level pressure, shortwave and downward longwave radiation, and precipitation. Upward longwave radiation is dependent on SST. Secondly, these monthly mean changes are added to CORE v2 atmospheric surface fields for the corresponding month and year for the 1951–2000 period used for ROMS-Hist. Finally, the bulk formula is used to calculate the projected surface fluxes of momentum, and sensible and latent heat, with the parameters determined in the second step. The model sea surface salinity is restored to the values determined in the second step. We also apply this approach to the initial and lateral boundary conditions. The initial conditions for the future runs are also generated by adding the changes in temperature and salinity between January 1951 and January 2051 in the CMIP5 models to the initial condition of ROMS-Hist. The initial sea level and velocities are set to zero in all future runs. The lateral boundary conditions for the future runs are created by adding changes in monthly mean temperature, salinity and velocity between 2051–2100 and 1951–2000 period in the CMIP5 models to the respective fields in SODA2.2.4 in the period 1951–2000. We call the three ROMS future runs forced by the MIROC-ESM, CSIRO-Mk3.6.0, and GFDL-CM3 variables ROMS-MIROC, ROMS-CSIRO, and ROMS-GFDL, respectively. The last 20 years of historical run and of all future runs are used in the following analyses.

2.4 Regional sea level

To focus on the regional distribution, we analyze RSL, which is the sea level at each grid point minus the global mean (e.g., Yin et al. 2010; Zhang et al. 2014). The RSL in the CMIP5 models is given by,

$$h'_{CM}(x, y, t) = h_{CM}(x, y, t) - \bar{h}_{CM}^G(t) \quad (1)$$

where h_{CM} is the sea level in a climate model (zos in CMIP5), \bar{h}_{CM}^G is its global mean

sea level, t is time, and x and y are the zonal and meridional coordinates, respectively. Because the ROMS domain does not cover the global, and thus we use the corresponding CMIP5 climate models' global mean as substitute. The RSL in ROMS simulations is defined using the following formula,

$$h'_{ROMS}(x, y, t) = h_{ROMS}(x, y, t) - \bar{h}_{CM}^G(t) - (\bar{h}_{ROMS}^D(t) - \bar{h}_{CM}^D(t)) \quad (2)$$

where the h_{ROMS} is the sea level output of ROMS, \bar{h}_{CM}^G is the corresponding CMIP5 model's global mean, \bar{h}_{ROMS}^D and \bar{h}_{CM}^D are the means over the current model domain (110°E–100°W, 5°N–50°N) in ROMS and the CMIP5 models, respectively.

2.5 Observational data

The ROMS-Hist is compared with the following observational data. The maps of weekly absolute dynamic height are compiled from the TOPEX/Poseidon, ERS-1/2, Jason-1, and Envisat altimeter observations on a $1/3^\circ \times 1/3^\circ$ Mercator spatial resolution grid from January 1993 to December 2000, distributed by the Archiving, Validation and Interpretation of Satellite Oceanographic Data (AVISO) (Ducet et al. 2000). The absolute dynamic height products are computed with consistent sea level anomaly and mean dynamic topography field (Rio and Hernandez 2004).

3. Results

3.1 Comparison of ROMS-Hist and observations

To evaluate the capability of the ROMS downscaling, the time-mean surface velocity obtained from the three CMIP5 models, ROMS-Hist, and satellite data are compared in Figure 3. Generally, all three CMIP5 models show a broad Kuroshio Current and KE without fine details. In particular, the Kuroshio and the KE are much weaker. In contrast, ROMS-Hist captures the salient features of western boundary currents, including the strong Kuroshio and its extension. It should be noted that ROMS-Hist fails to produce some observed features, as expected for an eddy-permitting model (e.g., Kagimoto and Yamagata, 1997; Sumata et al. 2012; Shu et al. 2013). The Kuroshio Current overshoots northward along the Japanese eastern coast by about 40°N and the KE is mainly formed roughly along 38°N with a minor eastward flow around 30°N . In the satellite observations, the Kuroshio Current separates from the coast and turns into the KE around 35°N . The modeled extension around 30°N is associated with the separation of the Kuroshio Current from the coast to the east of Kyushu. Similar deficiency found in some eddy-permitting models. For example, Shu et al. (2013) established a global eddy-permitting ocean-ice coupled model with a horizontal resolution of 0.25° by 0.25° on the basis of Modular Ocean Model version 4 (MOM4) and Sea Ice Simulator (SIS). They also found that the separation points of the Kuroshio from the eastern coast of Japan are too northward in their model. Sumata et al. (2010) performed a hindcast experiment using an eddy-permitting ocean ecosystem model based on COCO v4.3, with grid spacing of 0.28125° (zonal) and 0.1875° (meridional). The model has 51 vertical layers including a bottom boundary layer, and 7 layers which are embedded in the sigma-coordinate. The KE shifted northward by 2–3 degree as our model. These deficiency may be improved for an eddy-

resolving model of 0.1° resolution (e.g., Masumoto et al. 2004), which requires one-order larger computation resources. The systematic discrepancy between the ROMS-Hist and observation should be taken into account in interpreting downscaled future changes.

The different surface current structures among the CMIP5 climate models, ROMS-Hist, and observation are reflected in differences of SSH, because the SSH gradient is closely related to the surface current speeds through the geostrophy. Figure 4 shows that ROMS-Hist exhibits sharp SSH gradients across the Kuroshio Current and the KE as observed, although the CMIP5 climate models have broad, weak gradients especially over the KE. Proper reproduction of sharp SSH gradients is important in sea level changes, because shifts in SSH fronts can produce large sea level changes. Figure 5 compares the standard deviation of interannual SSH variations of ROMS-Hist and satellite observation. The standard deviation calculation is based on monthly anomalies defined as deviations from the mean values over 8 year period 1993–2000, for both the ROMS-Hist and satellite observations. In ROMS-Hist, high interannual variance is concentrated within a narrow latitudinal band along the mean KE front, which is similar to the observed SSH, although the KE shifted northward as aforementioned. On the other hand, in the ROMS-Hist, there is another maximum in SSH variance located south of the Honshu, which is not obvious in the satellite observations, this is related to the large meander of Kuroshio south of Honshu in ROMS-Hist.

Another deficiency in the CMIP5 climate models is that the three straits connecting the Japan Sea either to the North Pacific Ocean or to marginal seas, Such as the Tsushima, Tsugaru, and Soya Straits, are not properly resolved. The Tsugaru Strait is closed in MIROC-ESM and CSIRO-Mk3.6.0, whereas the Soya Strait is closed in GFDL-CM3. Furthermore, some straits are too wide in those models. Therefore, future flow changes

through the straits cannot be examined using these climate models. However, the volume transports through three straits can be estimated in ROMS downscaling, albeit with limited accuracy in reproducing the volume transports in the present climate. Many measurements revealed that a part of the East China Sea water enters the Japan Sea through the Tsushima Strait, and the same amount water exits through the Tsugaru and Soya Straits. The observed volume transports are 2.6 Sv ($1 \text{ Sv} = 10^6 \text{ m}^3 \text{ s}^{-1}$) (Fukudome et al. 2010), 1.6 Sv (Ito et al. 2003), and 0.7 Sv (Fukamachi et al. 2010) through the Tsushima, Tsugaru, and Soya Straits, respectively, whereas they are 1.8, 1.9, and -0.1 Sv in ROMS-Hist simulations (Fig. 20). Hence, ROMS-Hist underestimate the Tsushima Strait throughflow by 30%, overestimate the Tsugaru Strait throughflow by 20%, and exhibits opposite flow direction through the Soya Strait.

3.2 Regional sea level changes around Japan

In this section we investigate how large the RSL changes around Japan are by the end of 21st century under the RCP8.5 scenario. Figure 6 shows the projected changes in mean RSL around Japan during 2081–2100 period relative to 1981–2100 period in the three CMIP5 models and in the corresponding ROMS downscaling simulations. The three CMIP5 models project RSL rises in the subtropical gyre east of Japan, with a maximal RSL rise of 44, 37, and 27 cm in MIROC-ESM, CSIRO-Mk3.6.0, and GFDL-CM3, respectively.

The RSL changes in the ROMS simulations exhibit finer structures and higher magnitudes than those in the CMIP5 models, with some similarities among different downscaling simulations (Fig. 6). The downscaled RSLs commonly exhibit strong, bullseye-like RSL rise maxima centered on 41°N, 142°E to the east of the Tsugaru Strait

and zonally aligned three maxima along 37°N between 140°E and 160°E . A comparison of these RSL rise pattern with the surface current in the end of the 21st century (Fig. 7) and the end of the 20th century (Fig. 3) reveals that the RSL rise to the east of the Tsugaru Strait is related to the enhanced northward intrusion of the Kuroshio Current along the eastern coast of Japan. The RSL rise along 37°N is associated with the northward shift of the KE in ROMS-MIROC and ROMS-GFDL. The relatively large RSL rise at 30°N and 40°N is related to the substantial weakening of the eastward current along 30°N found in ROMS-Hist and to the enhanced eastward currents around 40°N . The ROMS downscaling exhibits larger RSL rise maxima than the CMIP5 models; The RSL rise maxima reaches 73, 74, and 85 cm to the east of Japan in ROMS-MIROC, ROMS-CSIRO, and ROMS-GFDL, respectively. It should be noted that in all ROMS simulations, the RSL rise contours close in the ocean interior, and RSL rises larger than 30 cm are limited to the seaward of the continental shelf off the Japanese archipelago, so that the high off-shore RSL rise would not reach the coast of Japan.

To better understand the relationship between the off-shore and coastal RSL changes, we examine the meridional distribution of the RSL rise zonally averaged over 145°E – 155°E and that on the Japanese eastern coast simulated by the CMIP5 models (Fig. 8) and the ROMS downscaling (Fig. 9). We selected the coastal RSL as the RSL at the ocean grid located next to the easternmost land grid of Japan at each latitude. In all CMIP5 models and ROMS simulations, the RSL changes along the eastern coast of Japan are generally one-third or less of the RSL rise maxima off the eastern coast of Japan.

Figure 10 shows RSL rises at all coastal grid points along Honshu Island, which is connected to Kyushu and Shikoku islands forming one island in the ROMS simulations, and Hokkaido Island. The coastal RSL changes during 2081–2100 period relative to

1981–2000 period derived directly from the three CMIP5 models and those obtained from ROMS downscaling are shown in Figs. 10a and 10b for the eastern and western coasts, respectively. The projected RSL rise during 2081–2100 period relative to 1981–2000 period along Honshu is 22–29, 8–15, and 8–18 cm in ROMS-MIROC, ROMS-CSIRO, and ROMS-GFDL, respectively. An important feature is that the differences in RSL changes between downscaling simulations and the corresponding CMIP5 models are less than 10 cm along Honshu coast. This means that if a 10 cm discrepancy is allowed at the maximum, we can use climate model outputs directly to assess RSL rise along Honshu coast. The smaller differences in coastal RSL than in off-shore RSL between the ROMS downscaling and climate models are probably caused by coastally trapped shelf waves. These waves tend to average sea level along the coast, resulting in roughly constant coastal sea level, which is given by the average of sea level at the northern and southern ends of the island (Liu et al. 1999). Along-coast sea level distributions, which are smaller than those off shore, are associated with friction and nonlinearity (Tsujino et al. 2008). The northward decrease in RSL changes on the western Honshu coast may be consistent with the northward propagation of shelf waves with damping along the route by emitted Rossby waves toward the west. The discrepancies between ROMS simulations and the CMIP5 models for MIROC-ESM and CSIRO-Mk3.6.0 are large on the Hokkaido coast, because the Tsugaru Strait is closed in these two climate models, they cannot include RSL changes associated with changes in the Tsugaru Strait throughflow.

The largest downscaled RSL rise occurs on the Sanriku coast in all ROMS simulations (Fig. 10), consistent with Fig. 9, which shows the coastal RSL rise maximum is located just south of 40°N. The maximal RSL increase is 29, 15, and 18 cm in ROMS-MIROC, ROMS-CSIRO, and ROMS-GFDL, respectively. This maximal RSL rise is

apparently related to the aforementioned northward shift of the separation latitude of the Kuroshio Current from the eastern coast. Considering the northward overshooting bias of the Kuroshio Current in ROMS-Hist, we suggest that the maximal coastal RSL rise would occur in a region near the actual separation of the Kuroshio Current from the eastern coast around 35°N, if unbiased downscaling can be conducted with these climate models. This is consistent with Sasaki et al. (2014) who showed that the decadal meridional migration of the KE causes a coastal sea level variability maximum in the Tokai area, which is located just south of the Kuroshio separation latitude.

Although the RSL rises in the CMIP5 models and in ROMS downscaling are generally similar along Honshu, they can be substantially different at the islands separated from Honshu, because sea levels at those islands are not affected by the averaging effects of coastal waves. Here, we examine sea level change at Okinawa Island, because extremely high sea levels have occurred there (Tokeshi and Yanagi, 2003), suggesting that it is important to project the RSL rise at Okinawa Island in the future warming climate. Although Okinawa Island is too small to be represented as an island in the current ROMS downscaling simulations, sea level changes at the island would be well approximated by the modeled sea level changes at that location. Figure 11 shows the projected RSL changes at Okinawa Island during 2081–2100 period relative to 1981–2000 period in the three CMIP5 models and the corresponding ROMS simulations. Both ROMS-MIROC and ROMS-CSIRO project high RSL rises at Okinawa Island of 30 and 29 cm, respectively, which are as much as or larger than the RSL rise maxima on the Honshu coast. The difference between CSIRO-Mk3.6.0 and ROMS-CSIRO is 16 cm, exceeding the aforementioned maximal discrepancy of 10 cm along the Honshu coast between the CMIP5 climate model and ROMS downscaling.

To clarify if the rising trend of RSL in the future is faster than that of current climate or not, we examined the RSL changes for 20 years from 1981–2000 and from 2081–2100. Figure 12 shows the time series of the annual mean RSL at a point on the Sanriku coast (39°N, 142°E), where the highest RSL rise along the Honshu coast is found as shown in Figure 10a, and at Okinawa Island (26.75°N, 128°E). It found that the RSL at the point on the Sanriku tend to rise faster during 2081–2100 period than during 1981–2000 period. However, the rate of RSL rise at Okinawa Island do not change so much between 2081–2100 period and 1981–2000 period.

3.3 Three-dimensional oceanic changes

As revealed by previous studies, the spatial distributions of RSL rise in the western North Pacific are related to the upper ocean changes (Sakamoto et al. 2005; Sato et al. 2006; Suzuki and Ishii 2011a; Sueyoshi and Yasuda 2012). In this section, we investigate future changes below the surface in the western North Pacific in our ROMS downscaling simulations in order to understand the relationships between these changes and RSL rise around Japan.

Sea level changes accompanied by density changes are represented by dynamic height (DH). DH is a commonly used parameter that can be calculated in terms of temperature and salinity by the Eq.3 (Gill 1982) with reference to 2000 dbar.

$$\Delta DH = \frac{1}{g} \int_{2000}^0 (v_s(S, T, p) - v_s(35 \text{ psu}, 0 \text{ }^\circ\text{C}, p)) dp \quad (3)$$

here S is salinity, T is temperature, g is the acceleration of gravity (9.8 m s^{-2}), and v_s is specific volume, given by the reciprocal of in situ density, and the anomaly of specific volume is defined as the specific volume related to that at the same pressure for salinity of 35 psu and temperature of 0 °C. Thus, DH is defined as the vertical integration of the

specific volume anomaly from the pressure of 2000 to 0 dbar (at the surface). For consistency with the RSL rise, regional dynamic height (RDH) is defined in a similar manner to the RSL definition (Eq. 2), as given by

$$\Delta DH'_{ROMS} = \Delta DH_{ROMS} - \overline{\Delta DH}_{CM}^G - (\overline{\Delta DH}_{ROMS}^D - \overline{DH}_{CM}^D) \quad (4)$$

where the ΔDH_{ROMS} is DH calculated by the ROMS outputs, $\overline{\Delta DH}_{CM}^G$ is the corresponding CMIP5 model's global mean DH, $\overline{\Delta DH}_{ROMS}^D$ and $\overline{\Delta DH}_{CM}^D$ are the DH means over the North Pacific ROMS domain in ROMS and the CMIP5 models, respectively.

Figure 13 shows the RDH changes during 2081–2100 period relative to 1981–2000 period obtained from the three ROMS downscaling simulations. The comparison of the RDH changes (Figs. 13(a)–(c)) and RSL rises (Figs. 6(d)–(f)) indicate that the RDH changes very well reproduce the major features of RSL rises described in the previous section, including RSL rises associated with the KE changes.

We examine how deep the signatures related to RSL rises penetrate downward. Figure 14 shows projected changes in mean eastward velocity zonally averaged from 145°E to 155°E in a meridional-vertical cross section across the KE during 2081–2100 period relative to 1981–2000 period in the ROMS simulations. The zonal velocity changes are consistent with the aforementioned KE changes. For example, a dipole consisting of positive (negative) eastward velocity changes to the north (south) of the KE axis at 37°N in ROMS-MIROC and ROMS-GFDL are associated with the northward migration of the KE axis. These zonal velocity changes mainly occur in the upper 1000 m, and penetrate down to 2000 m as more clearly seen in vertical profile at the latitudes of local maxima and minima (Fig. 15). The vertical penetration may suggest that this pattern is unlikely to be caused by heat or fresh water fluxes at the surface. This is because

such thermohaline flux changes would cause temperature and salinity changes primarily limited to major water masses such as subtropical mode water at depths of 300–400 m or shallower (Suzuki and Ishii 2011b). Therefore, these changes are probably forced by wind stress changes (e.g., Sakamoto et al. 2005; Sato et al. 2006; Sueyoshi and Yasuda 2012). The velocity changes in ROMS-CSIRO penetrate to shallower depth than in the other two models.

Here we investigate the impact of wind stress on the distribution of sea level. The linear response of the ocean circulation to surface wind stress curl can be computed by the Sverdrup balance (Sverdrup 1947), the Sverdrup stream function can be derived by the following equation, zonal integral of wind stress curl westward from the eastern boundary along each latitude,

$$\psi(\lambda, \phi) = -\frac{1}{\rho_0 \beta} \int_{\lambda}^{\lambda_E} k \cdot (\nabla \times \boldsymbol{\tau}) R \cos \phi d\lambda' \quad (5)$$

Where ψ is the Sverdrup stream function, λ is the longitude, ϕ is the latitude, λ_E is the longitude of the eastern boundary, $\rho_0 = 1027 \text{ kg m}^{-3}$ is the reference sea-water density, β is the beta parameter representing the meridional gradient of the Coriolis parameter, R is the radius of the earth, k is the unit vector in the vertical direction, and $\nabla \times \boldsymbol{\tau}$ is the surface wind stress curl. $\psi(\lambda_E)$, the Sverdrup stream function value at the eastern boundary, is set to zero. A positive Sverdrup stream function is associated with a positive RSL change. The mean Sverdrup stream function changes during 2081–2000 period relative to 1981–2000 period is shown in Figure 16(d)–(f). All ROMS simulations commonly show that the positive Sverdrup stream function changes east of Japan are caused by the negative wind stress curl changes in the North Pacific (Figure 16(a)–(c)). However, there are some model-model differences. For instance, in ROMS-MIROC, Sverdrup stream function and RSL increase in a latitude band centered near 37°N.

Therefore, the RSL changes in this model is determined by wind stress changes as aforementioned. However, in ROMS-CSIRO and ROMS-GFDL, the differences of patterns of Sverdrup stream function changes and RSL changes may be explained by the nonlinearity response of the ocean circulation to surface wind stress curl.

As indicated by Eq. (3), DH change is totally given by specific density changes, which are shown in Figure 17. As expected, specific volume changes exhibit signature of northward migration of KE in ROMS-MIROC and ROMS-GFDL, characterized by upward convex around 37°N from the surface down to 1400 m depth. In ROMS-CSIRO, near surface increase of specific volume is much more prominent than the other two models, and contours of changes are roughly parallel to contours of mean values. These features in ROMS-CSIRO suggest that water mass changes may play a more important role in this model than in the others. Furthermore, ROMS-CSIRO exhibits the strongest surface stratification among three downscaling models. Although Yin et al (2010) suggested that ocean strong stratification can make the RSL gradient much steep associated with the subtropical gyre, this hypothesis does not explain the zonal velocity changes in this model shown in Figure 14.

It is interesting to decompose the RDH changes shown in Figs. 13(a)–(c) into thermosteric and halosteric components. The decomposition methods are described in Eqs (6) and (7) (Landerer et al. 2007; Zhang et al. 2014).

$$\Delta DH_T(0,2000) = \frac{1}{g} \int_{2000}^0 (v_s(35psu, T, p) - v_s(35 psu, 0 \text{ }^\circ\text{C}, p)) dp \quad (6)$$

$$\Delta DH_S(0,2000) = \frac{1}{g} \int_{2000}^0 (v_s(S, 0 \text{ }^\circ\text{C}, p) - v_s(35 psu, 0 \text{ }^\circ\text{C}, p)) dp \quad (7)$$

Here, ΔDH_T and ΔDH_S are the thermosteric and halosteric DH, respectively. The calculation of regional thermosteric and halosteric DH is similar to that of RDH given in

Eq. (4). Figure 13(d)-(f) and Figure 13(g)-(i) show the regional thermosteric and halosteric contributions, respectively, to RDH changes during 2081–2100 period relative to 1981–2000 period. The sum of these two components recover the RDH changes well (Figure 13(j)–(l)). Thus, although the specific density is a nonlinear function of temperature, salinity and depth, its nonlinearity is weak with respect to temperature and salinity differences caused by the climate change. In all ROMS simulations, thermosteric components dominate the RDH change between 30°N and 40°N. Smaller halosteric components contribute to producing a larger RDH to the south than to the north. Consequently, the thermosteric component gives the major RDH, and thus the major RSL rise features, whereas halosteric component helps to produce the overall meridional gradient in the RSL rise.

The different thermosteric and halosteric DH changes are associated with the different vertical distribution of temperature and salinity changes. Figures 18 and 19 show the vertical distribution of projected changes in time-mean potential temperature and salinity, respectively, zonally averaged over 145°E–155°E across KE during 2081–2100 period relative to 1981–2000 period. As expected, both temperature warming and salinity freshening are larger near the surface than at depth. Freshening may be due to enhanced water cycle so that precipitation minus evaporation will increase in regions where the climatological precipitation is larger than the climatological evaporation, known as “wet get wetter” (Held and Soden 2006; Chou et al. 2009). The temperature changes are generally large to the north, while opposite is true for salinity changes. The aforementioned KE’s northward migration in ROMS-MIROC and ROMS-GFDL is associated with the downward convex of temperature change and upward convex of salinity change around 37°N. An interesting difference between the temperature and

salinity changes around 37°N is that the former penetrate deeper than the latter. This is probably due to the fact that the meridional gradient of climatological mean temperature is strong at the KE from the surface down to 2000 m depth, whereas the meridional gradient of mean salinity is strongly only shallower than 800 m. Therefore, meridional migration of mean oceanic structures associated with the KE can yield deep penetrating changes in temperature but relatively shallow changes in salinity.

The spatial structure of sea level changes may be associated with changes of throughflow transport via the Tsugaru, Tsushima and Soya Straits, because differences in sea level between the upstream and downstream of a strait strongly constraints throughflows (Ohshima 1994; Lyu and Kim 2005; Tsujino et al. 2008). Figure 20 shows the time-mean volume transports during 1981–2000 period and 2081–2100 period through the Tsushima, Tsugaru, and Soya Straits in ROMS downscaling. All transports through the straits will increase in the future warming climate. ROMS-CSIRO projects a much larger increase in the transport of each strait compared with the other two downscaling simulations. This is probably because ROMS-CSIRO projects a negative RSL rise in the subpolar gyre (Fig. 6), in contrast to the positive RSL rise in the other two models. The negative RSL rise in the subpolar gyre, combined with the positive RSL rise in subtropical gyre is associated with the larger increase in SSH difference between the subpolar and subtropical gyres in ROMS-CSIRO than in other two models.

Apart from the context of sea level rise, an interesting parameter in ROMS downscaling is SST, which is important in feedback from the ocean to the atmosphere (e.g., Small et al. 2008; Chelton and Xie 2010) and marine ecosystems (e.g., Abdul-Aziz et al. 2011). Figures 21 (a)–(c) shows that the three climate models exhibit the maximal SST increase to the east of the Tsugaru Strait, which suggests that the northward migration

of the Kuroshio Current affects these models. The maximal SST warming in ROMS downscaling is reminiscent of the SST change in the climate model (Figs. 21(d)–(f)), as downscaling simulations also have maximal SST warming just east of the Tsugaru Strait. However, the magnitude of the maximal SST warming in ROMS-GFDL is as high as 13 °C, nearly 1.5 times larger than that in the corresponding climate model (9 °C). In addition, ROMS-CSIRO exhibits enhanced SST warming relative to the climate model, whereas maximal SST warming in ROMS-MIROC is only slightly larger than in the climate model. The localized maximal SST change is probably related to the larger northward intrusion of the Kuroshio Current at the end of the 21st century than that at the end of the 20th century in surface current velocities (Figs. 3 and 7) and in SSTs (Fig. 22). Although the present downscaling model has a bias in separation latitude of the Kuroshio Current from the eastern coast of Japan described in section 3.1, the commonly found maximal SST increase occurring around the northernmost latitude of the coastal Kuroshio Current reaches in the climate models and ROMS downscaling simulations suggest that possible future changes of the Kuroshio Current may result in large SST change around its separation latitude, which is about 36°N in observations. The strong SST warming is apparently related to the SST front, the strongest meridional gradient of climatological SSTs.

4. Summary and Discussion

In this paper, we investigated the future RSL rise in the western North Pacific by conducting dynamical downscaling by using ROMS with eddy-permitting $0.25^{\circ} \times 0.25^{\circ}$ resolution. To evaluate the worst cases of RSL rise at the end of 21st century around Japan, we selected climate models that have highest RSL rise near Japan (Fig. 1a), MIROC-ESM, CSIRO-Mk3.6.0, and GFDL-CM3, under the highest greenhouse gas emission scenario, RCP8.5. The dynamical downscaling are performed for two epochs: the historical run (1950–2000) and the future run (2051–2100). The historical run, ROMS-Hist, is forced by the air-sea fluxes calculated by using COREv2 data. Three future runs—ROMS-MIROC, ROMS-CSIRO, and ROMS-GFDL—are forced with an atmospheric field constructed by adding the difference between the CMIP5 parameters of the 21st and 20th century to the present forcing fields used in ROMS-Hist.

The ROMS downscaling captures finer structures and stronger magnitudes for the RSL changes than those in the CMIP5 models. The downscaled changes commonly exhibit strong, bullseye-like RSL rise maxima centered at 41°N , 142°E to the east of the Tsugaru Strait and three zonally aligned maxima along 37°N between 140°E and 160°E (Fig. 6). The projected RSL rise maxima during 2081–2100 period relative to 1981–2000 period reach 73, 74, and 85 cm, in ROMS-MIROC, ROMS-CSIRO, and ROMS-GFDL, respectively (Fig. 6).

Most importantly, ROMS downscaling enable us to access the coastal regional sea-level change around Japan, which is limited in the CMIP5 models due to their coarse resolution. All ROMS downscaling commonly show that the coastal RSL rises are smaller than the off-shore RSL rises (Figs. 6 and 9), which is consistent with Sato et al. (2006). The projected RSL rise along the Honshu coast during 2081–2100 period relative to

1981–2000 period is 22–29, 8–15, and 8–18 cm in ROMS-MIROC, ROMS-CSIRO, and ROMS-GFDL, respectively, which are generally one-third or less of the RSL rise maxima off the eastern coast of Japan. The largest downscaled RSL rise occurs on the Sanriku coast in all models (Figs. 9 and 10). The projected RSL change along the Hokkaido coast during 2081–2100 period relative to 1981–2000 period is 17–21, -8–1, -1–7 cm in ROMS-MIROC, ROMS-CSIRO, and ROMS-GFDL, respectively (Fig. 10). On the other hand, the ranges of RSL changes along the Honshu coast are small in all ROMS downscaling, probably due to shelf waves, which play a role in spatial averaging associated with wave's propagation along the coast (Fig. 10). The RSL rising in all ROMS downscaling tend to be faster in the end of the 21st century than those in the end of the 20th century along the Honshu coast (Fig. 12a). Although the CMIP5 models underestimate off-shore RSL rise maxima substantially than ROMS downscaling (Figs. 6, 8, and 9), the discrepancies between the climate models and ROMS downscaling are less than 10 cm along the Honshu coast (Fig. 10). The discrepancies are relatively large on Hokkaido coast between the downscaled RSL changes and those in CMIP5 models for MIROC-ESM and CSIRO-Mk3.6.0 (Fig. 10), because the closed Tsugaru Strait in these climate models does not allow RSL difference associated with the Tsugaru throughflow changes. Since averaging effects of the shelf waves do not contribute to the sea level for islands separated from Honshu, larger RSL changes can occur for some islands than those along the Honshu with larger difference between the climate models and ROMS downscaling. At Okinawa Island, the RSL changes are nearly 30 cm in ROMS-MIROC and ROMS-CSIRO, which is higher than the changes along the Honshu coast. The difference in RSL rise at Okinawa Island between ROMS-CSIRO and CSIRO-Mk3.6.0 exceeds 10 cm (Fig. 11).

The three-dimensional structures of oceanic changes are important in understanding the mechanism of off-shore RSL changes. In ROMS-MIROC and ROMS-GFDL, the RSL changes to the east of Japan are accompanied by the zonal velocity changes across the KE in the upper 1000 m, penetrating down to 2000 m (Figs. 14 and 15). This pattern suggests that these changes are probably caused by wind stress changes (e.g., Sakamoto et al. 2005; Sato et al. 2006; Sueyoshi and Yasuda 2012) rather than caused by heat or freshwater fluxes at the surface. In ROMS-CSIRO, near surface increase of specific volume is much more prominent than the other two models (Fig. 17), indicating relatively larger importance of the water mass changes in this model than in other two models. The RDH changes relative to 2000 dbar reproduce major features of RSL rises very well, including RSL rises associated with the KE changes (Fig. 13). All ROMS simulations commonly show that the thermosteric changes give the major features of RDH and thus major RSL changes, while halosteric components contribute to producing the overall meridional gradients in RSL changes (Fig. 13). The different thermosteric and halosteric component are associated with the different distribution of temperature and salinity changes (Figs. 18 and 19). The meridional migration of oceanic structures associated with KE northward shift yields deep penetrating changes in temperature while relatively shallow changes in salinity associated with the climatological mean distribution of respective parameters.

Other factors that are not taken into account in the present downscaling simulation can influence RSL changes, such as the inverse barometer effect, glacial isostatic adjustment (GIA), gravitational changes resulted from land ice melting and changes of land water storage, and climate model drift (Church et al. 2013; Slangen et al. 2014). The inverse barometer effect, which yields an absolute sea level change less than 3 cm over

the North Pacific in all models, is much smaller than the steric and land ice contributions and hence can be neglected. Based on the IPCC AR5, the GIA and gravitation changes has a relatively small effect around Japan. Climate drifts of the three CMIP5 climate models, which are evaluated using the pre-industry control run, are small for RSL in the western North Pacific, and can be ignored.

In order to obtain information useful for society, it is important to evaluate total sea level rise, which can be obtained by the RSL change through downscaling and the global mean sea level rise. Contributions to global mean sea level change include glaciers, land ice and land water storage contributions, thermal expansion contribution, and GIA (Church et al. 2013; Slangen et al. 2014). The GIA effect on the global mean sea level is small (-3 cm in 100 years) (Peltier and Luthcke 2009). The glaciers, land ice, and land water storage contributions to the global mean sea level rise are nearly 16, 16, and 4 cm, respectively, in 2081–2100 relative to 1986–2005 for RCP8.5 in IPCC AR5 (Table 13.SM.1, Church et al. 2013). The thermal expansion components during 2081–2100 relative to 1981–2000 under RCP8.5 are 43, 29, and 36 cm, in MIROC-ESM, CSIRO-Mk3.6.0, and GFDL-CM3, respectively¹. As a result, the global mean sea level rise are 79, 65, and 72 cm during 2081–2100 relative to 1981–2000 under RCP8.5 in MIROC-ESM, CSIRO-Mk3.6.0, and GFDL-CM3, as a minor reference period difference of 20th century, i.e., 1986–2005 in AR5 and 1980–2000 in the present study, can be ignored. Consequently, the coastal sea level rise in total, which is given by the addition of the RSL increase documented in section 3.2 and the global mean sea level rise, are expected to be

¹ Globally averaged sea-level due to thermal expansion (thermosteric component) is estimated with a variable, *zostoga*, in CMIP5. However, *zostoga* is not available for GFDL-CM3, and thus we use another variability, *zossga*, (global average steric sea level change). For 18 CMIP5 models, both *zostoga* and *zossga* are available and the difference between them are small (less than 1.5% for 100 year difference for 15 models, Fig. 22).

101–108, 73–80, and 80–90 cm in ROMS-MIROC, ROMS-CSIRO, and ROMS-GFDL, respectively.

An important result in the present study is that the present downscaling reveals that the discrepancy along the Honshu coast between the CMIP5 climate models and corresponding ROMS downscaling is less than 10 cm. Thus, with 10 cm uncertainty, the RSL change along the Honshu coast can be directly evaluated from CMIP5 climate model outputs. This allows the coastal RSL rise to be evaluated with a larger number of climate models (nearly 40), and the probability of sea level changes to be evaluated considering the uncertainties among climate models.

At eddy-permitting $0.25^\circ \times 0.25^\circ$ resolution here, ROMS-Hist exhibits some bias, such as the overshoot of the Kuroshio Current and the northward shift of KE compared with observations. Although we have taken these biases into account in interpreting the downscaled sea level changes, it is not possible to identify the specific locations and magnitudes of the largest coastal sea level rise. Hence, the largest coastal RSL rise on the Sanriku coast should be carefully interpreted with the model bias. This location almost corresponds to the northward overshooting bias of the Kuroshio Current in ROMS-Hist, but in reality the Kuroshio Current separates from the eastern coast around 35°N . Therefore, a reasonable interpretation may be the maximal coastal RSL rise would occur around 35°N , consistent with Sasaki et al. (2014) who found the largest sea level rise variability in the Tokai region, which is near the real separation of the Kuroshio Current, for past decadal sea level variability. The biases mentioned above are a common problem for the non-eddy-resolving model (Sumata et al. 2010; Shu et al. 2013). In order to overcome these biases, downscaling with eddy-resolving resolution $0.1^\circ \times 0.1^\circ$ may be required. This should be an important research in future, because Tokyo, the most densely

city and the capital of Japan, is located near from the separation point of the Kuroshio at 35°N. The computation cost of this resolution is about 16 times larger than that in our experiments, which we expect will become feasible for a number of laboratories in the next decade.

Acknowledgement

I would like to express my most sincere thanks to my academic supervisor, Professor Shoshiro Minobe, for his many invaluable suggestions, untiring support, and contributions towards my research. Without his guidance and support through the past years, this thesis would not have been possible to accomplish. Specially, I would like to express my gratitude to Lecturer Yoshinori Sasaki for his valuable time in helping me with ROMS experimental equipment and in providing me lots of constructive suggestions and comments. Sincere thanks also go all the members of my PhD committee, Dr. Tatsuo Suzuki and Profs. Masato Furuya, Masaru Inatsu, and Hanna Na for their useful comments and suggestions. Also many thanks go to Professor Humio Mitsudera for providing the numerical computation resource of the simulator in the Institute of Low Temperature Science, Hokkaido University. I am grateful to the labmates, both present and former, for making the lab run so smoothly and enjoyable. Finally, I would like to thank my parents for their support throughout these years.

References

- Abdul-Aziz OI, Mantua NJ, Myers KW (2011) Potential climate change impacts on thermal habitats of Pacific salmon (*Oncorhynchus* spp.) in the North Pacific Ocean and adjacent seas. *Can J Fish Aquat Sci* 68(9):1660-1680. doi: 10.113/F2011-079
- Ådlandsvik B (2008) Marine downscaling of a future climate scenario for the North Sea. *Tellus* 60A:451-458. doi: 10.1111/j.1600-0870.2008.00311.x
- Antonov JI, Seidov D, Boyer TP, Locarnini RA, Mishonov AV, Garcia HE, Baranova OK, Zweng MM, Johnson DR (2010) World Ocean Atlas 2009. In: Levitus S (eds) Vol. 2. Salinity, NOAA Atlas NESDIS 68, Government Printing Office, Washington, pp. 184
- Bindoff NL et al (2007) Observations: Oceanic climate change and sea level. In: Solomon S et al (eds) *Climate Change 2007: The Physical Science Basis. Contribution of Working Group I to the Fourth Assessment Report of the Intergovernmental Panel on Climate Change*, Cambridge University Press, Cambridge
- Carton JA, Giese BS (2008) A reanalysis of ocean climate using Simple Ocean Data Assimilation (SODA), *Mon Weather Rev* 136(8):2999-3017
- Cazenave A, Cozannet GL (2013) Sea level rise and its coastal impacts. *Earth's Future* 2:15-34. doi: 10.1002/2013EF000188
- Chamberlain MA, Sun CJ, Matear RJ, Feng M, Phipps SJ (2012) Downscaling the climate change for oceans around Australia. *Geosci Model Dev* 5:1177-1194
- Chelton DB, Xie SP (2010) Coupled ocean-atmosphere interaction at oceanic mesoscales. *Oceanog* 23(4):52-69
- Chou C, Neelin JD, Chen CA, Tu JY (2009) Evaluating the “rich-get-richer” mechanism in tropical precipitation change under global warming. *J Climate* 22:1982-2005
- Church JA et al (2013) Sea Level Change. In: Stocker TF et al (eds) *Climate Change*

2013: The Physical Science Basis. Contribution of Working Group I to the Fifth Assessment Report of the Intergovernmental Panel on Climate Change, Cambridge University Press, Cambridge

Collier MA, Jeffrey SJ, Rotstayn LD, Wong KK, Dravitzki SM, Moseneder C, Hamalainen C, Syktus JJ, Suppiah R, Antony J, El-Zein A, Artif M (2011) The CSIRO-Mk3.6.0 Atmosphere-Ocean GCM: Participation in CMIP5 and data publication. Int Congr Modell Simul, MODSIM 2011, Perth

Curchitser EN, Haidvogel DB, Hermann AJ, Dobbins EL, Powell TM, Kaplan A (2005) Multi-scale modeling of the North Pacific Ocean: Assessment and analysis of simulated basin-scale variability (1996-2003). J Geophys Res 110(C11021). doi: 10.1029/2005JC002902

Ducet N, Le Traon PY, Reverdin G (2000) Global high resolution mapping of ocean circulation from TOPEX/Poseidon and ERS-1/2. J Geophys Res 105(19):477-498

Fairall CW, Bradley EF, Hare JE, Grachev AA, Edson JB (2003) Bulk parameterization of air-sea fluxes: Updates and verification for the COARE algorithm. J Clim 16:571-591

Fukamachi Y, Ohshima KI, Ebuchi N, Bando T, Ono K, Sano M (2010) Volume transport in the Soya strait during 2006-2008. J Oceanogr 66:685-696

Fukudome K, Yoon JH, Ostrovskii A, Takikawa T, Han IS (2010) Seasonal volume transport variation in the Tsushima warm current through the Tsushima Straits from 10 years of ADCP observations. J Oceanogr 66:539-551

Gill AE (1982) Atmosphere-ocean dynamics. Academic Press, Harcourt Place, London, pp. 215

Griffies SM et al (2005) Formulation of an ocean model for global climate simulations.

Ocean Sci 1:45-79

Griffies SM, Winton M, Donner LJ et al (2011) The GFDL CM3 coupled climate model: Characteristics of the ocean and sea ice simulations. *J Clim* 24:3520-3544. doi: 10.1175/2011JCLI3964.1

Haidvogel DB, Arango HG, Hedstrom K, Beckmann A, Malanotte-Rizzoli P, Shchepetkin AF (2000) Model evaluation experiments in the North Atlantic basin: Simulations in nonlinear terrain-following coordinates. *Dyn Atmos Oceans* 32:239-281

Han W, Moore AM, Levin J, Zhang B, Arango HG, Curchitser E, Lorenzo ED, Gordon AL, Lin J (2009) Seasonal surface ocean circulation and dynamics in the Philippine Archipelago region during 2004-2008. *Dyn Atmos Oceans* 47:114-137

Hanson S, Nicholls R, Ranger N, Hallegatte S, Corfee-Morlot J, Herweijer C, Chateau J (2011) A global ranking of port cities with high exposure to climate extremes. *Clim Change* 104:89-111. doi: 10.1007/s10584-010-9977-4

Held IM, Soden BJ (2006) Robust responses of the hydrological cycle to global warming. *J Climate* 19:5686-5699

Ito T, Togawa O, Ohnishi M, Isoda Y, Nakayama T, Shima S, Kuroda H, Iwahashi M, Sato C (2003) Variation of velocity and volume transport of the Tsugaru warm current in the winter of 1999-2000. *Geophys Res Lett* 30(13):1678. doi:10.1029/2003GL017522

Jeffrey SJ, Rotstayn LD, Collier MA, Dravitzk SM, Hamalaien C, Moeseneder C, Wong KK, Syktus JI (2013) Australia's CMIP5 submission using the CSIRO Mk3.6 model. *Aust Meteorol Oceanogr J* 60:37-47

Kagimoto T, Yamagata T (1997) Seasonal transport variations of the Kuroshio: An

- OGCM simulation. *J Phys Oceanogr* 27:403-418.
- Landerer FW, Jungclaus JH, Marotzke J (2007) Regional dynamic and steric sea level change in response to the IPCC=A1B scenario. *J Phys Oceanogr* 37:296-312
- Large WG, McWilliams JC, Doney SC (1994) Oceanic vertical mixing: A review and a model with a nonlocal boundary layer parameterization. *Rev Geophys* 32:363-404
- Large WG, Yeager S (2008) The global climatology of an interannually varying air-sea flux data set. *Clim Dyn* 33:341-364. doi: 10.1007/s00382-008-0441-3
- Lee T, Waliser DE, Li JF, Landerer FW, Gierach MM (2013) Evaluation of CMIP3 and CMIP5 wind stress climatology using satellite measurements and atmospheric reanalysis products. *J Clim* 26:5810-5826. doi: 10.1175/JCLI-D-12-00591.1
- Liu Y, Xie L, Morrison JM, Kamykowski D (2013) Dynamic downscaling of the impact of climate change on the ocean circulation in the Galápagos Archipelago. *Adv Meteorol* 2013:1-18
- Liu Y, Lee SK, Enfield DB, Muhling BA, Lamkin JT, Muller-Karger FE, Roffer MA (2015) Potential impact of climate change on the Intra-Americas Sea: Part-1. A dynamic downscaling of the CMIP5 model projections. *J Mar Sys* 148(2015):56-69
- Liu Z, Wu L (1999) Rossby wave-coastal kelvin wave interaction in the extratropics. part II: Formation of island circulation. *J Phys Oceanogr* 29:2405-2418
- Locarnini RA, Mishonov AV, Antonov JI, Boyer TP, Garcia HE, Baranova OK, Zweng MM, Johnson DR (2010) World Ocean Atlas 2009. In: Levitus S (eds) Vol. 1. Temperature, NOAA Atlas NESDIS 68, Government Printing Office, Washington, pp. 184
- Lorenzo ED, Schneider N, Cobb KM, Franks PJS, Chhak K et al (2008) North Pacific gyre oscillation links ocean climate and ecosystem change. *Geophys Res Lett*

35(L08607)

- Lowe JA, Gregory M (2006) Understanding projections of sea level rise in a Hadley Centre coupled climate model. *J Geophys Res* 111(C11014). doi: 10.1029/2005JC003421
- Marchesiello P, McWilliams JC, Shchepetkin A (2001) Open boundary conditions for long-term integration of regional oceanic model. *Ocean Modell* 3:1-20
- Masumoto Y, Sasaki H, Kagimoto T, Komori N, Ishida A, Sasai Y, Miyama T, Motoi T, Mitsudera H, Takahashi K, Sakuma H, Yamagata T (2004) A fifty-year eddy-resolving simulation of the world ocean -preliminary outcomes of OFES (OGCM for the Earth Simulator). *J Earth Sim* 1:35-56
- Meier HEM (2006) Baltic Sea climate in the late twenty-first century: A dynamical downscaling approach using two global models and two emission scenarios. *Clim Dyn* 27(1):39-68. doi: 10.1007/s00382-006-0124-x
- Moss RH, Edmonds JA, Hibbard KA et al (2010) The next generation of scenarios for climate change research and assessment. *Nature* 463:747-756. doi:10.1038/nature08823
- Nicholls RJ, Hanson S, Herweijer C, Patmore N, Hallegatte S et al (2008) Ranking port cities with high exposure and vulnerability to climate extremes: exposure estimates. OECD Publishing. <http://dx.doi.org/10.1787/011766488208>
- Ohshima KI (1994) The flow system in the Japan Sea caused by a sea level difference through shallow straits. *J Geophys Res* 99:9925-9940
- Oliver ECJ, Holbrook NJ (2014) Extending our understanding of South Pacific gyre “spin-up”: Modeling the East Australian Current in a future climate. *J Geophys Res Ocean* 119:2788-2805. doi: 10.1002/2013JC009591

- Peltier WR, Luthcke SB (2009) On the origins of Earth rotation anomalies: New insights on the basis of both “paleogeodetic” data and Gravity Recovery and Climate Experiment (GRACE) data. *J Geophys Res* 114(B11405). doi:10.1029/2009JB006352
- Rio MH, Hernandez F (2004) A mean dynamic topography computed over the world ocean from altimetry, in situ measurements, and a geoid model. *J Geophys Res* 109(C12032). doi:10.1029/2003JC002226
- Rotstayn LD et al (2010) Improved simulation of Australian climate and ENSO-related rainfall variability in a global climate model with an interactive aerosol treatment. *Int J Climatol* 30:1067-1088. doi: 10.1002/joc.1952
- Sakamoto TT, Hasumi H, Ishii M, Emori S, Suzuki T, Nishimura T, Sumi A (2005) Responses of the Kuroshio and the Kuroshio Extension to global warming in a high-resolution climate model. *Geophys Res Lett* 32(L14617). doi:10.1029/2005GL023384
- Sasaki YN, Minobe S, Miura Y (2014) Decadal sea-level variability along the coast of Japan in response to ocean circulation changes. *J Geophys Res Oceans* 119:266-275. doi: 10.1002/2013JC009327
- Sato Y, Yukimoto S, Tsujino H, Ishizaki H, Noda A (2006) Response of North Pacific ocean circulation in a Kuroshio-resolving ocean model to an Arctic Oscillation (AO)-like change in Northern Hemisphere atmospheric circulation due to greenhouse-gas forcing. *J Meteorol Soc Jpn* 84:295-309
- Sen Gupta A, Jourdain NC, Brown JN, Monselesan D (2013) Climate drift in the CMIP5 models. *J Clim* 26:8597-8615. doi: 10.1175/JCLI-D-12-00521.1
- Seo H, Miller AJ, Roads JO (2007) The scripps coupled ocean-atmosphere regional

- (SCOAR) model, with applications in the eastern Pacific sector. *J Clim* 20:381-402
- Seo GH, Cho YK, Choi BJ, Kim KY, Kim BG, Tak YJ (2014) Climate change projection in the Northwest Pacific marginal seas through dynamic downscaling. *J Geophys Res Oceans* 119:3497-3516. doi: 10.1002/2013JC009646
- Shchepetkin AF, McWilliams JC (2005) The regional oceanic modeling system (ROMS): A split-explicit, free-surface, topography-following-coordinate ocean model. *Ocean Modell* 9:347-404
- Shu Q, Qian FL, Song ZY, Yin XQ (2013) A comparison of two global ocean-ice coupled models with different horizontal resolutions. *Acta Oceanol Sin* 32(8):1-11
- Small RJ, deSzoeko SP, Xie SP, O'Neill L, Seo H, Song Q, Cornillon P, Spall M, Minobe S (2008) Air-sea interaction over ocean fronts and eddies. *Dyn Atmos Oceans* 45:274-319. doi: 10.1016/j.dynatmoce.2008.01.001
- Sueyoshi M, Yasuda T (2012) Inter-model variability of projected sea level changes in the western North Pacific in CMIP3 coupled climate models. *J Oceanogr* 68:533-543. doi: 10.1007/s10872-012-0117-9
- Sumata H, Hashioka T, Suzuki T, Yoshie N, Okunishi T, Aita MN, Sakamoto TT, Ishida A, Okada N, Yamanaka Y (2010) Effect of eddy transport on the nutrient supply into the euphotic zone simulated in an eddy-permitting ocean ecosystem model. *J Mar Sys* 83(2010):67-87. doi:10.1016/j.jmarsys.2010.07.002
- Sun CJ, Feng M, Matear RJ, Chamberlain MA, Craig P, Ridgway KR, Schiller A (2012) Marine downscaling of a future climate scenario for Australian boundary currents. *J Clim* 25(8):2947-2962. doi: 10.1175/JCLI-D-11-00159.1
- Suzuki T, Ishii M (2011a) Regional distribution of sea level changes resulting from enhanced greenhouse warming in the Model for Interdisciplinary Research on

- Climate version 3.2. *Geophys Res Lett* 38(L02601). doi:10.1029/2010GL045693
- Suzuki T, Ishii M (2011b) Long-term regional sea level changes due to variations in water mass density during the period 1981-2007. *Geophys Res Lett* 38(L21604). doi:10.1029/2011GL049326
- Sverdrup HU (1947) Wind-driven currents in a baroclinic ocean: with application to the equatorial currents of the Eastern Pacific. *Proc Nat Acad Sci USA* 33:318-326
- Tokeshi T, Yanagi T (2003) High sea level caused at Naha in Okinawa Island. *Oceanogr Japan* 12(4):395-405 (**in Japanese with English abstract**)
- Tsujino H, Nakano H, Motoi T (2008) Mechanism of currents through the straits of the Japan Sea: Mean state and seasonal variation. *J Oceanogr* 64:141-161
- Watanabe S, Hajima T, Sudo K et al (2011) MIROC-ESM 2010: model description and basic results of CMIP5-20c3m experiments. *Geosci Model Dev* 4:845-872. doi:10.5194/gmd-4-845-2011
- Yin J, Griffies SM, Stouffer RJ (2010) Spatial variability of sea level rise in twenty-first century projections. *J Clim* 23:4585-4607. doi:10.1175/2010JCLI3533.1
- Yin J (2012) Century to multi-century sea level rise projections from CMIP5 models. *Geophys. Res Lett* 39(L17709). doi:10.1029/2012GL052947
- Zhang XB, Church JA, Platten SM, Monselesan D (2014) Projection of subtropical gyre circulation and associated sea level changes in the Pacific based on CMIP3 climate models. *Clim Dyn* 43:131-144. doi:10.1007/s00382-013-1902-x

Figures

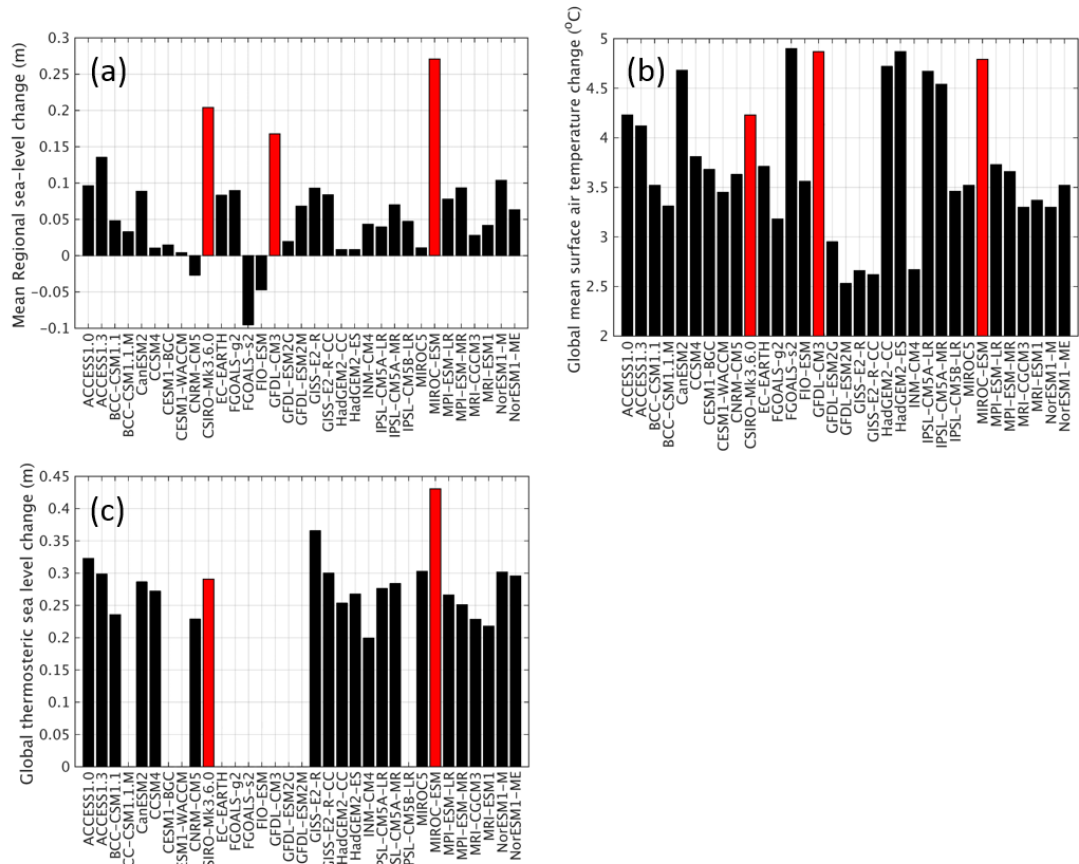


Fig. 1 (a) Projected RSL rises averaged over a domain bounded by 25°–40°N and 125°–180°E, (b) global mean surface air temperature changes during 2081–2100 relative to 1981–2000 for 33 CMIP5 climate models. (c) Global thermosteric sea level changes during 2081–2100 relative to 1981–2000 for 22 CMIP5 climate models. The three selected models are highlighted in red.

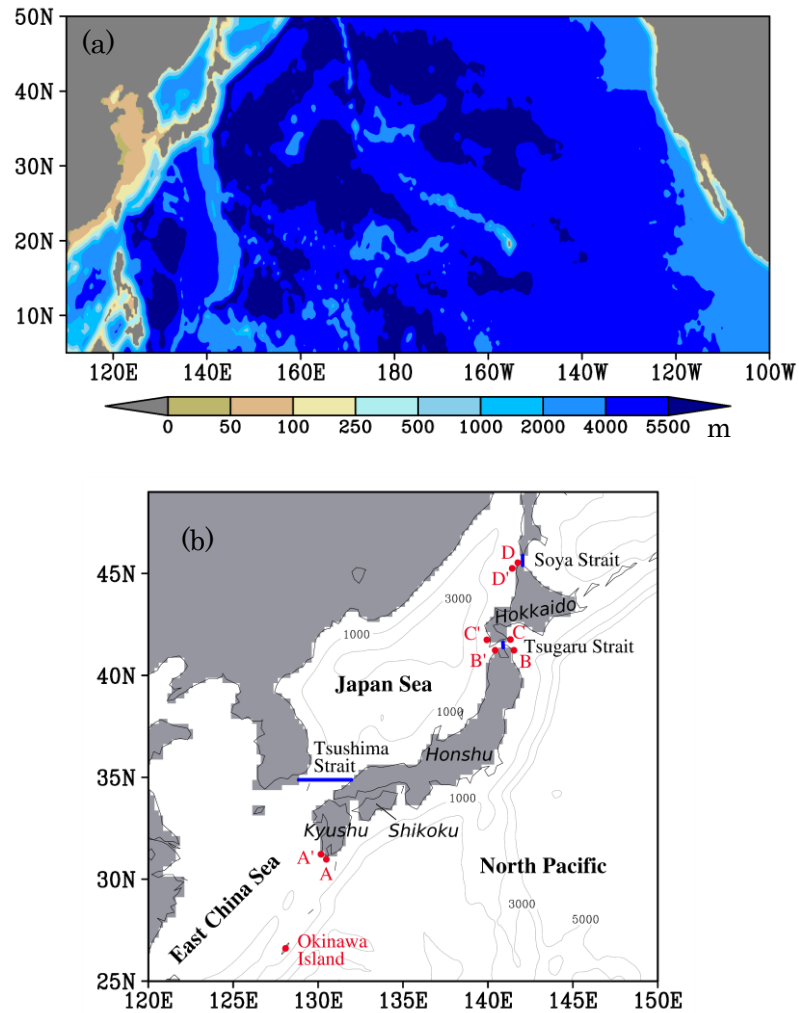


Fig. 2 (a) Oceanic bathymetry in ROMS model domain. (b) Topography around Japan from ROMS. Contours indicate bathymetric depths in meters, and gray areas indicate land mask. Blue lines denote the locations of the Tsushima, Tsugaru, and Soya Straits. Red dots denote the coastal stations used in Figure 9 and the Okinawa Island station (26.75°N , 128°E) in Figure 10.

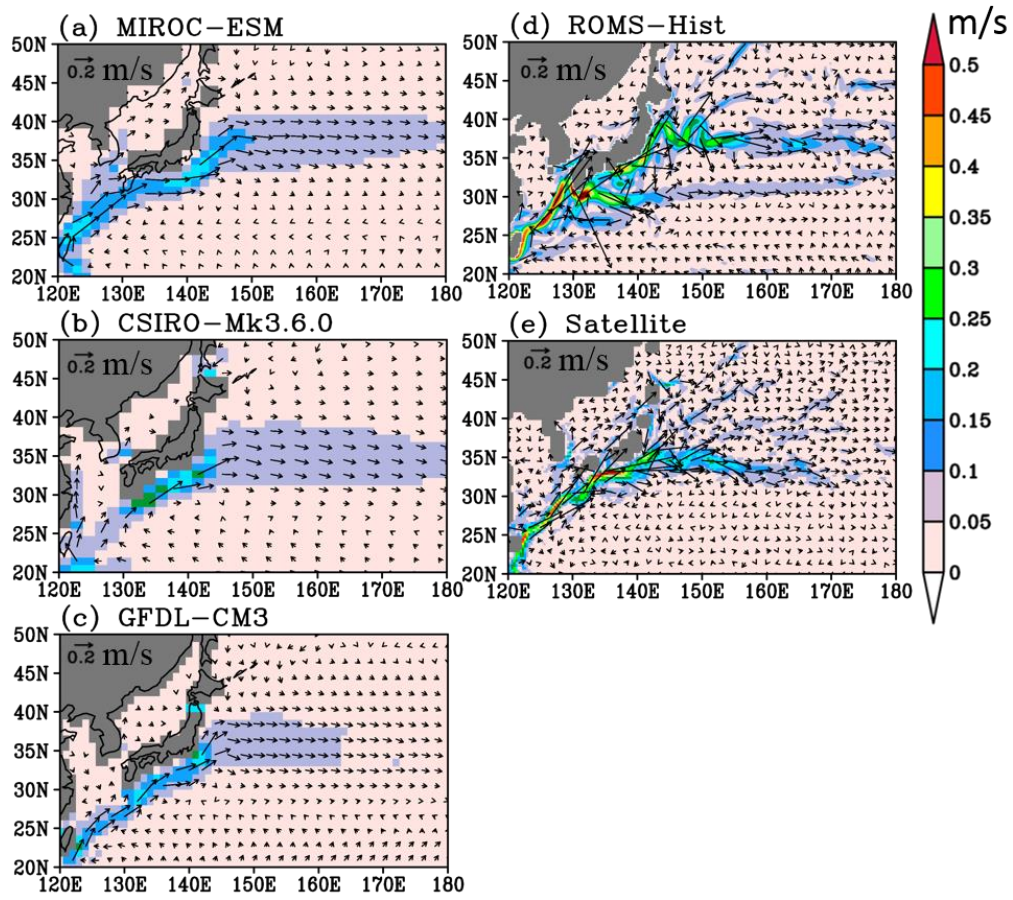


Fig. 3 Time-mean surface velocities (colors) and vector velocities (vectors) for 1993–2000 in the three selected CMIP5 climate models (a–c), the ROMS historical run (d), and the satellite-derived surface geostrophic currents (e).

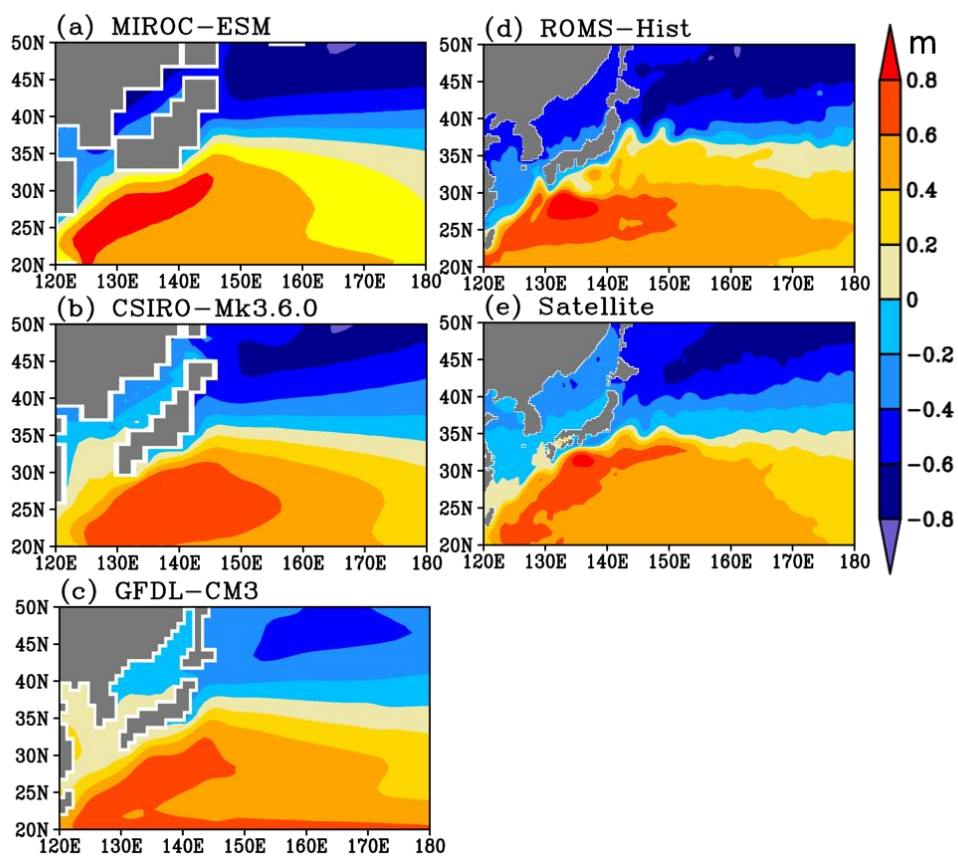


Fig. 4 Time-mean RSL for 1993–2000 period in three CMIP5 climate models (a–c), the ROMS historical run (d), and the satellite observations (e).

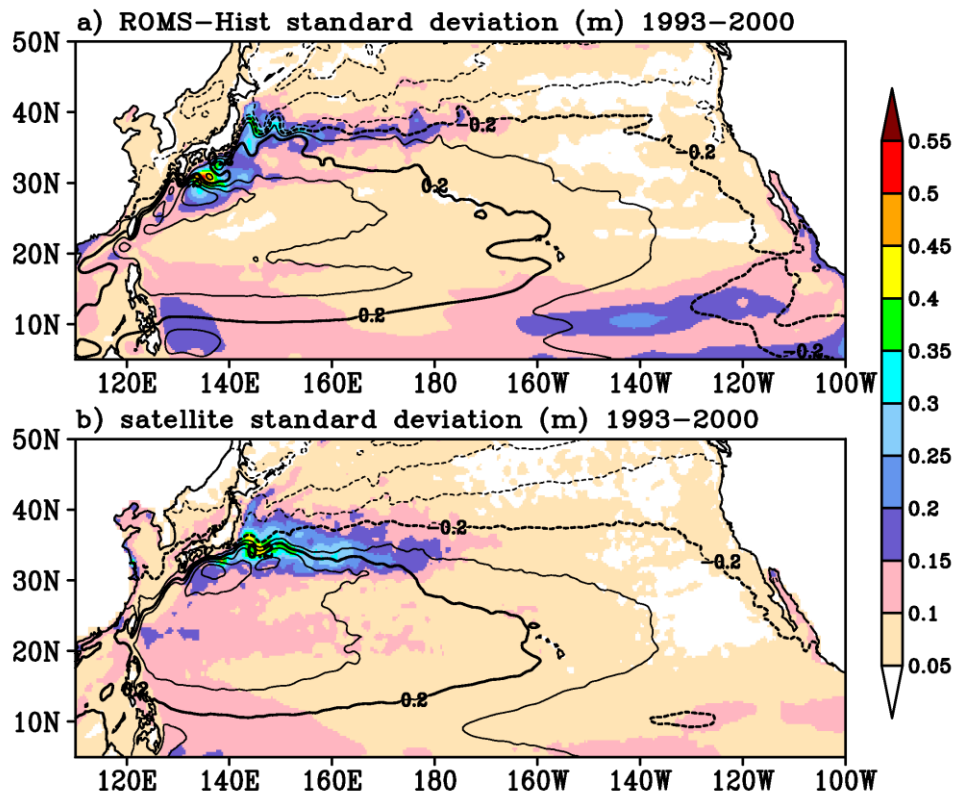


Fig. 5 (a) Standard deviation of SSH for the ROMS-Hist (colors, unit: m) and the mean absolute SSH (contours). (b) Same as in (a), but for the satellite observations.

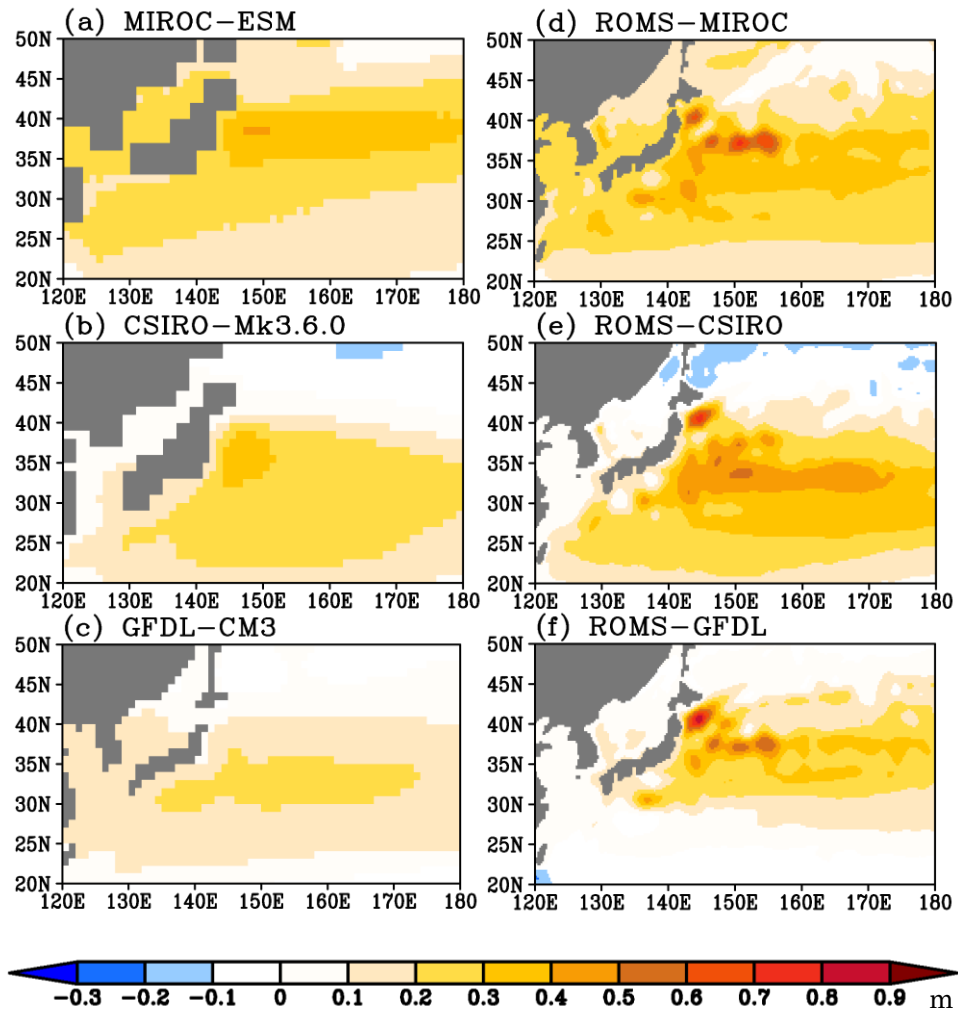


Fig. 6 Projected changes in mean RSL around Japan for 2081–2100 relative to 1981–2000 in (left) CMIP5 climate models under the RCP8.5 scenario and in (right) ROMS downscaling simulations. Top, middle, and bottom panels are for MIROC-ESM, CSIRO-Mk3.6.0, and GFDL-CM3, respectively.

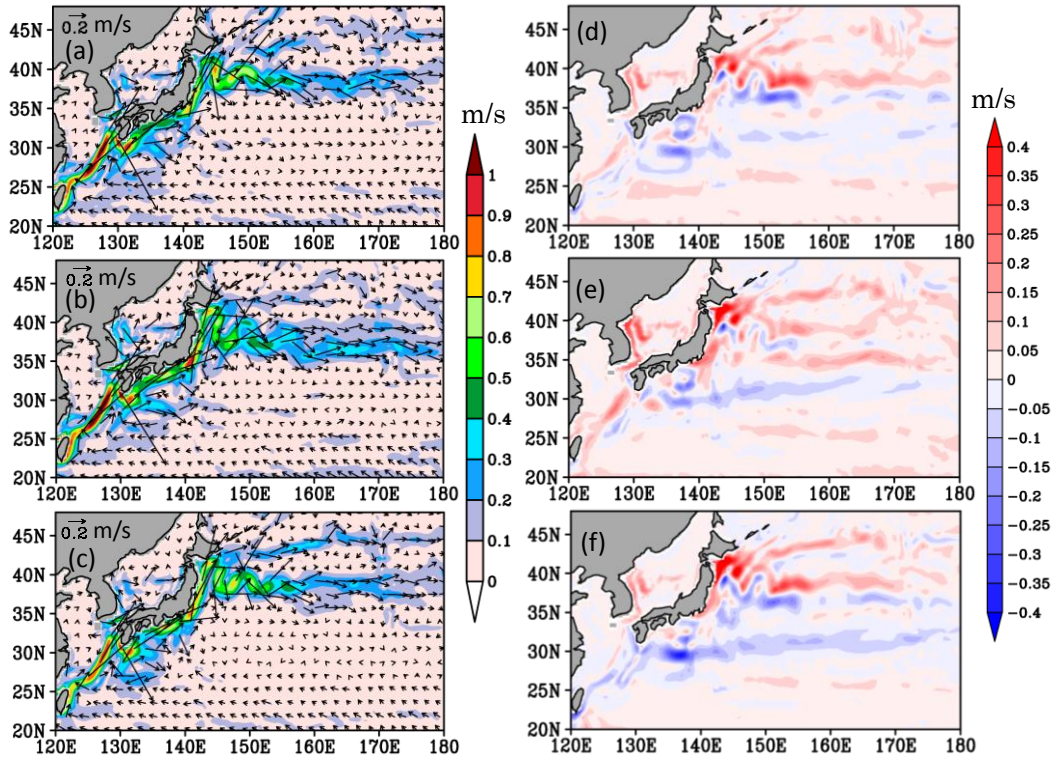


Fig. 7 (left) Time-mean surface absolute velocities (colors) and vector velocities (vectors) averaged over 2081–2100 period, and (right) Differences of mean surface absolute velocities between 2081–2100 period and 1981–2000 period, in (a, d) ROMS-MIROC, (b, e) ROMS-CSIRO, and (c, f) ROMS-GFDL.

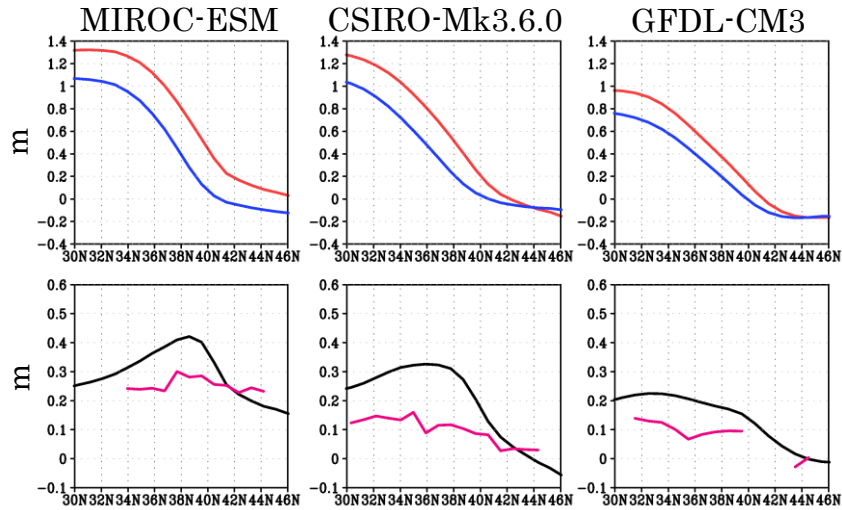


Fig. 8 (top) RSL zonally averaged from 145°E to 155°E and temporally averaged for 1981–2000 (blue) and 2081–2100 (red), and (bottom) projected RSL rise zonally averaged from 145° to 155°E (black) and projected Japanese eastern coastal RSL rise (purple) for 2081–2100 relative to 1981–2000 in (left) MIROC-ESM, (middle) CSIRO-Mk3.6.0, and (right) GFDL-CM3.

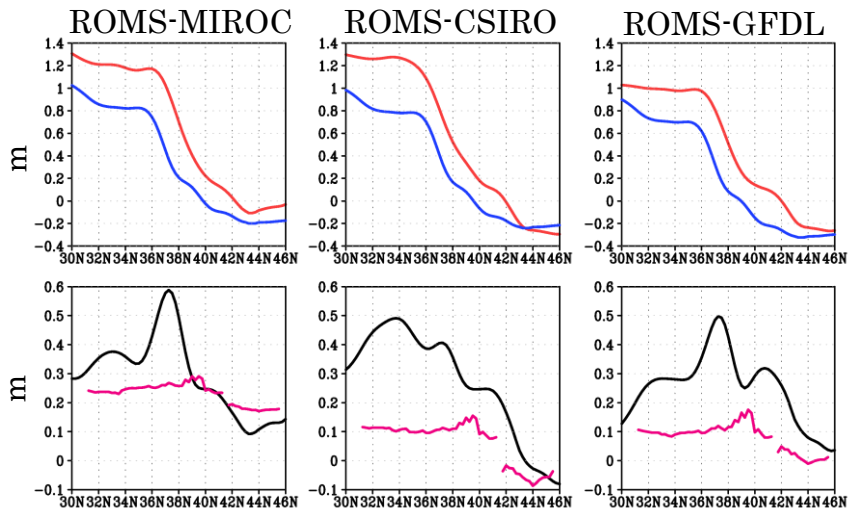


Fig. 9 (top) RSL zonally averaged from 145°E to 155°E and temporally averaged for 1981–2000 (blue) and 2081–2100 (red), and (bottom) projected RSL rise zonally averaged from 145° to 155°E (black) and projected Japanese eastern coastal RSL rise (purple) for 2081–2100 relative to 1981–2000 for the ROMS downscaling simulations with (left) ROMS-MIROC, (middle) ROMS-CSIRO, and (right) ROMS-GFDL.

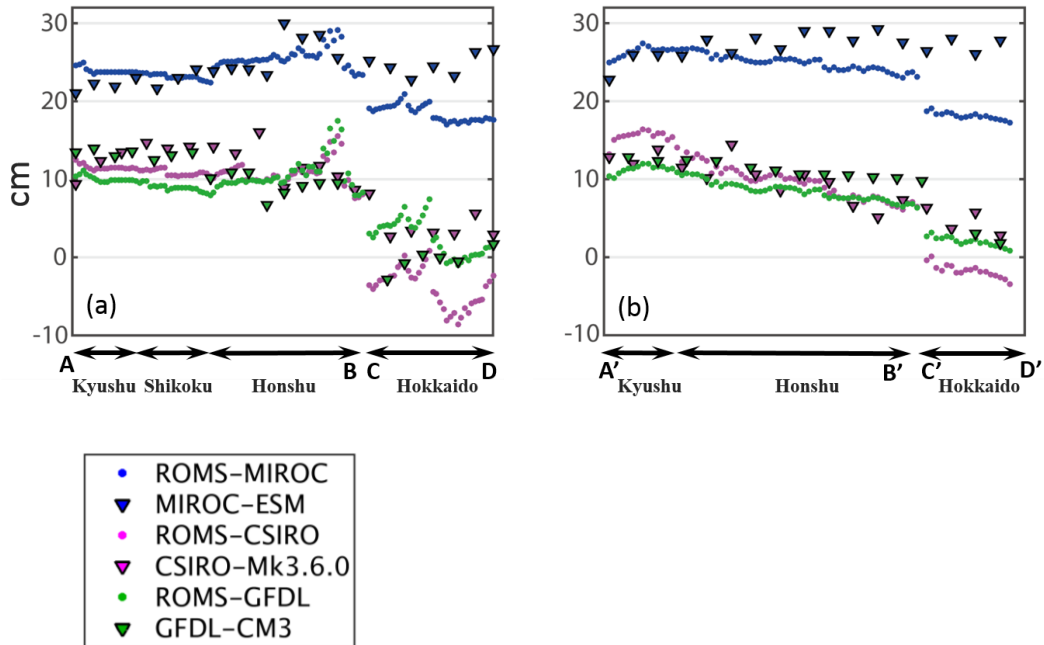


Fig. 10 Projected Japanese eastern (a) and western (b) coastal RSL rise for 2081–2100 relative to 1981–2000 in three CMIP5 models (triangles) and from ROMS simulations (dots), with MIROC-ESM and ROMS-MIROC (blue), CSIRO-Mk3.6.0 and ROMS-CSIRO (purple), and GFDL-CM3 and ROMS-GFDL (green). The labels A–D and A'–D' correspond to the location of the red dots shown in Fig. 2.

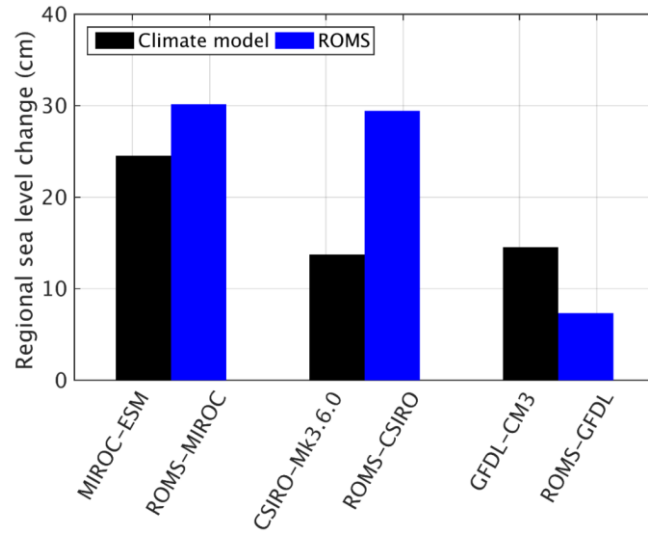


Fig. 11 Projected RSL rise (in centimeters) at Okinawa Island (26.75°N, 128°E, as shown in Fig. 2) during 2081–2100 relative to 1981–2000 in MIROC-ESM, CSIRO-Mk3.6.0, and GFDL-CM3 (black bars), and in the corresponding ROMS downscaling simulations (blue bars).

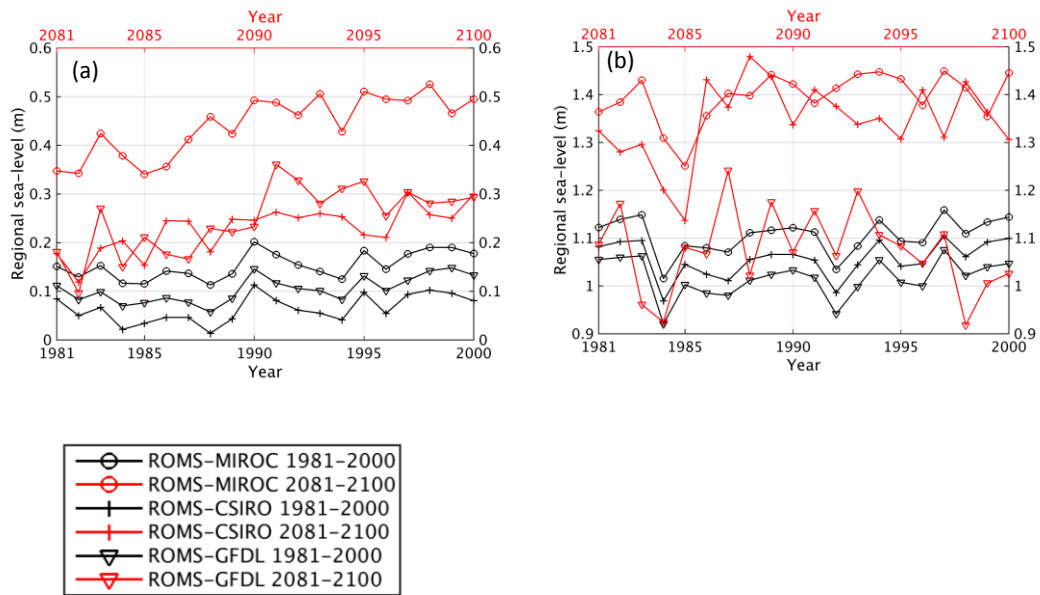


Fig. 12 Time series of annual mean RSL at (a) a point on Sanriku coast (39°N, 142°E) and at (b) Okinawa Island (26.75°N, 128°E) from 2081 to 2100 (red) and from 1981 to 2000 (black) in (circle) ROMS-MIROC, (cross) ROMS-CSIRO, and (triangle) ROMS-GFDL.

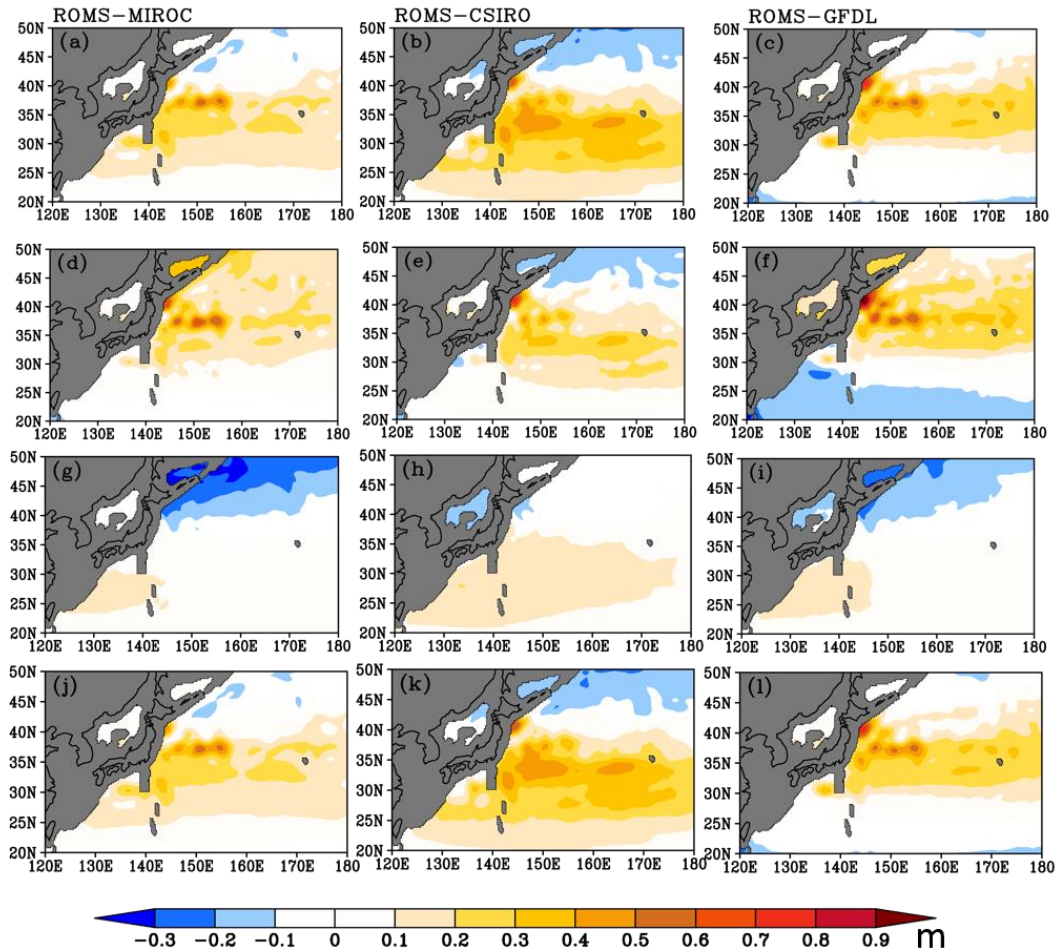


Fig. 13 (a–c) RDH changes with reference to 2000 dbar during 2081–2100 relative to the 1981–2000 period, (d–f) RDH changes due to the thermosteric component, and (g–i) RDH changes due to halosteric components, and (j–l) the sum of the thermosteric and halosteric components, in (left) ROMS-MIROC, (middle) ROMS-CSIRO, and (right) ROMS-GFDL.

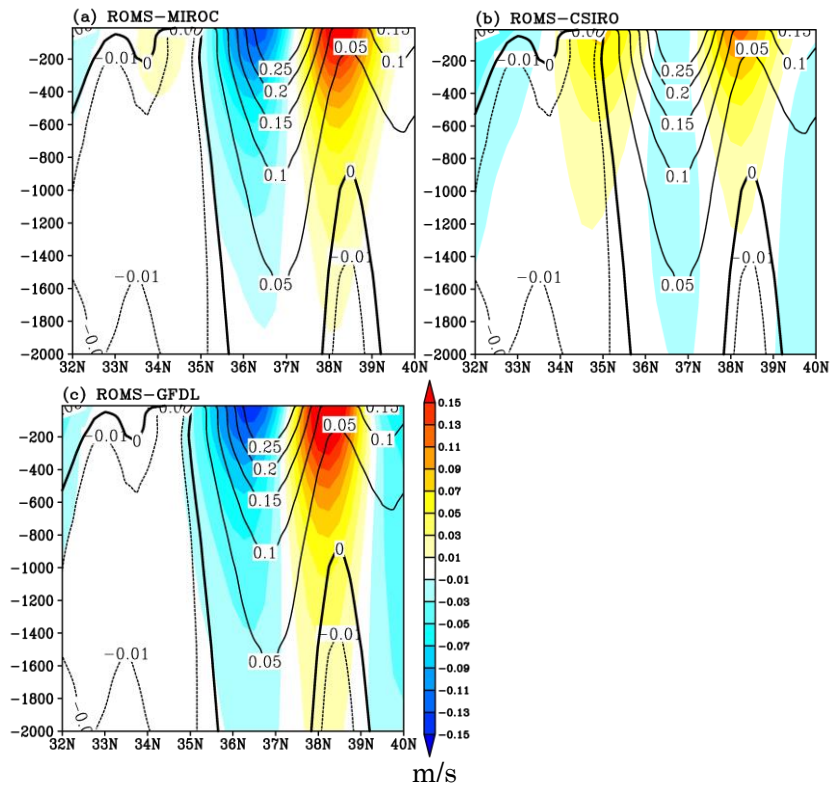


Fig. 14 Projected changes in mean eastward velocity zonally averaged from 145°E to 155°E for 2081–2100 relative to 1981–2000 (colors) in (a) ROMS-MIROC, (b) ROMS-CSIRO, and (c) ROMS-GFDL. Contours show the mean distribution for 1981–2000.

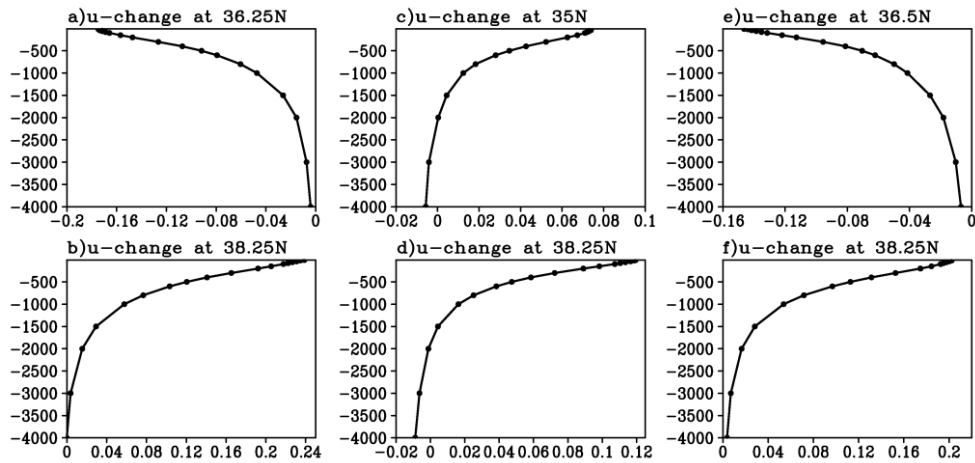


Fig. 15 Vertical profiles of projected changes in eastward velocity (in m s^{-1}) zonally averaged from 145°E to 155°E at the latitudes where the eastward velocity changes shown in Fig. 13 reach their local minima and maxima at the surface in ROMS-MIROC at (a) 36.25°N and (b) 38.25°N in ROMS-CSIRO at (c) 35°N and (d) 38.25°N , and in ROMS-GFDL at (e) 36.5°N and (f) 38.25°N .

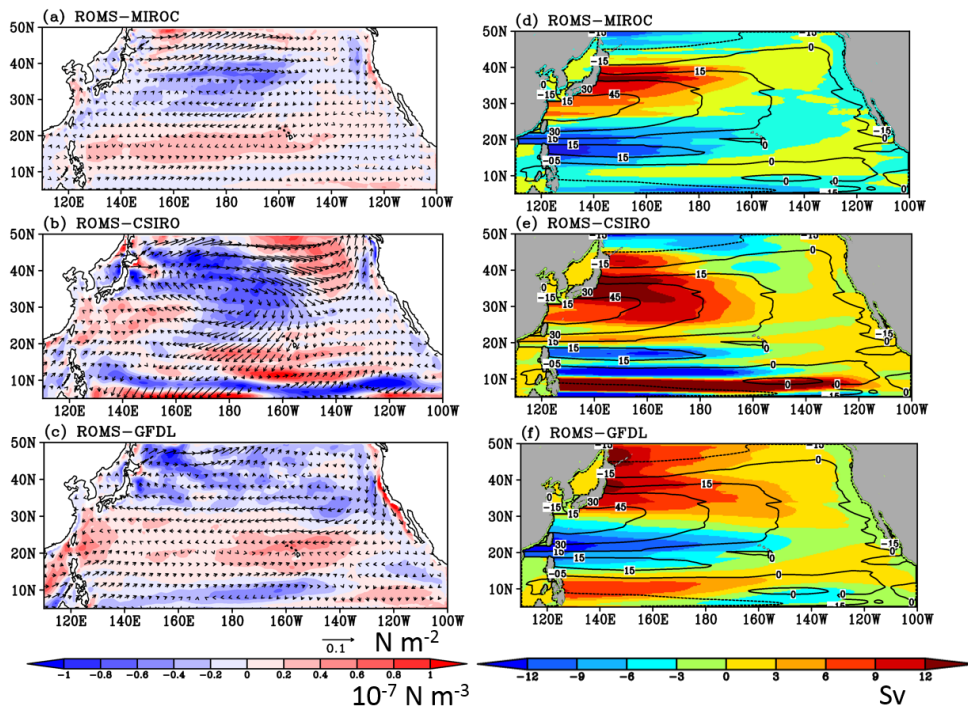


Fig. 16 (left) Projected changes in wind stress (N m^{-2} , vector) and its curl (10^{-7}N m^{-3} , color shading) for 2081–2100 relative to 1981–2000, and (right) Projected changes in Sverdrup stream function (Sv, color shading) for 2081–2100 relative to 1981–2000 along with their mean value for 1981–2000 (contours).

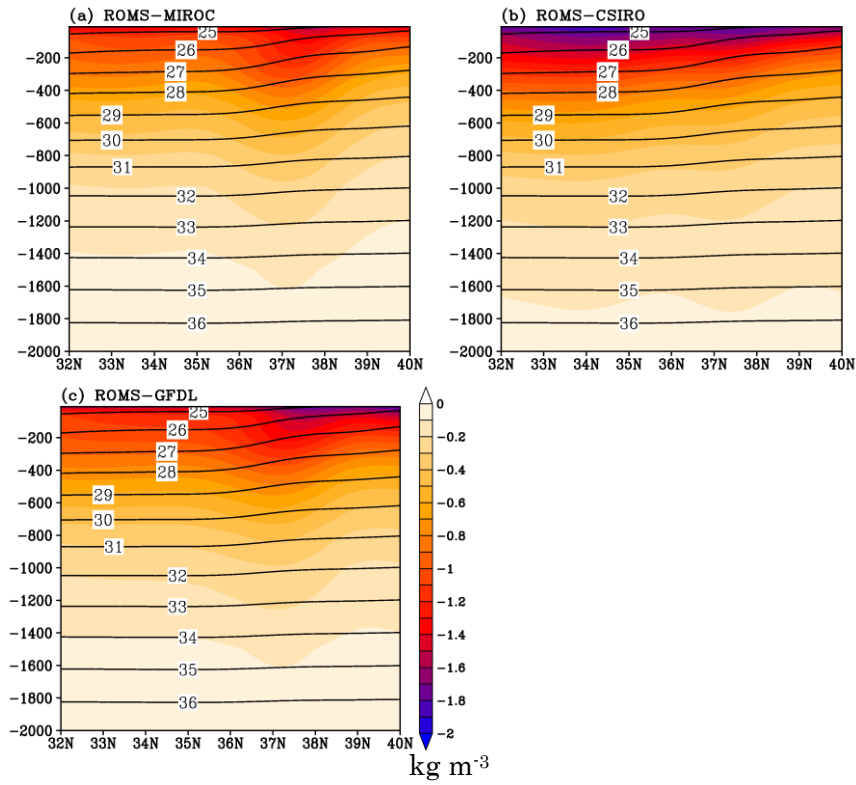


Fig. 17 Projected changes in in-situ density (color shading) zonal averaged from 145°E to 155°E during 2081–2100 period relative to 1981–2000 period (colors) in (a) ROMS-MIROC, (b) ROMS-CSIRO, and (c) ROMS-GFDL along with their mean value for the period 1981–2000 (minus 1000 kg m^{-3}).

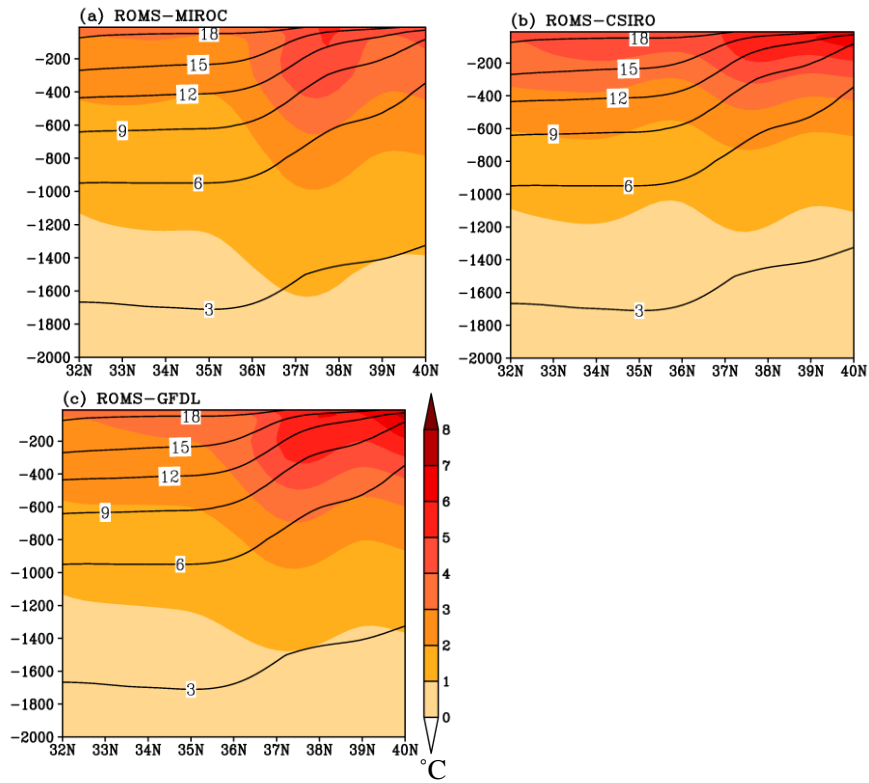


Fig. 18 Projected changes in potential temperature (in °C, color shading, meridional average has been removed at each depth) zonally averaged from 145°E to 155°E for 2081–2100 relative to 1981–2000 in (a) ROMS-MIROC, (b) ROMS-CSIRO, and (c) ROMS-GFDL along with their mean value for 1981–2000 (contours).

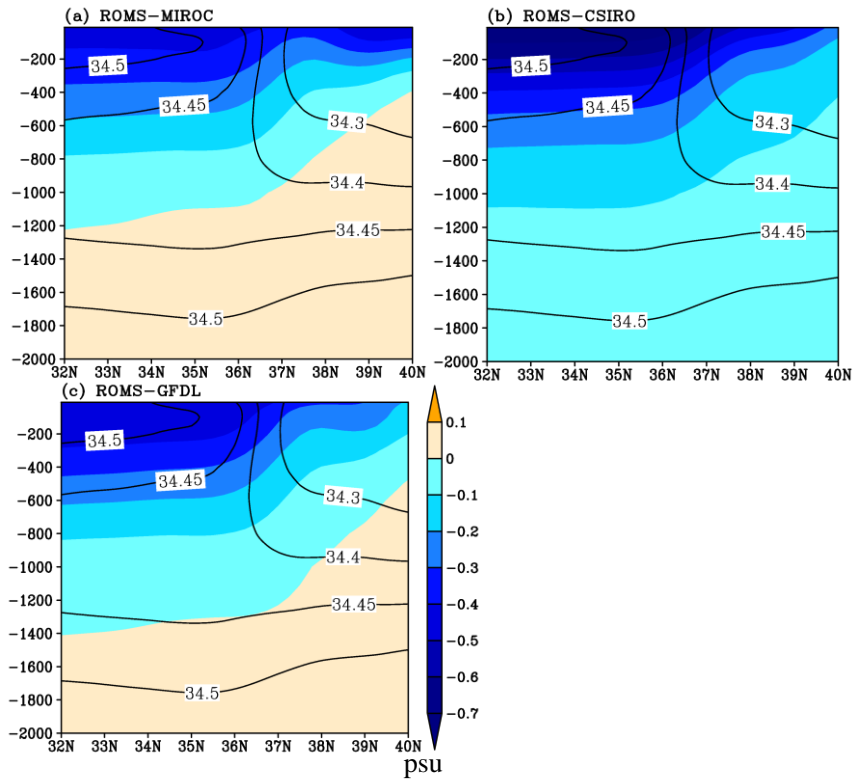


Fig. 19 Projected changes in salinity (in psu, color shading) zonally averaged from 145°E to 155°E for 2081–2100 relative to 1981–2000 in (a) ROMS-MIROC, (b) ROMS-CSIRO, and (c) ROMS-GFDL along with their mean value for 1981–2000 (contours).

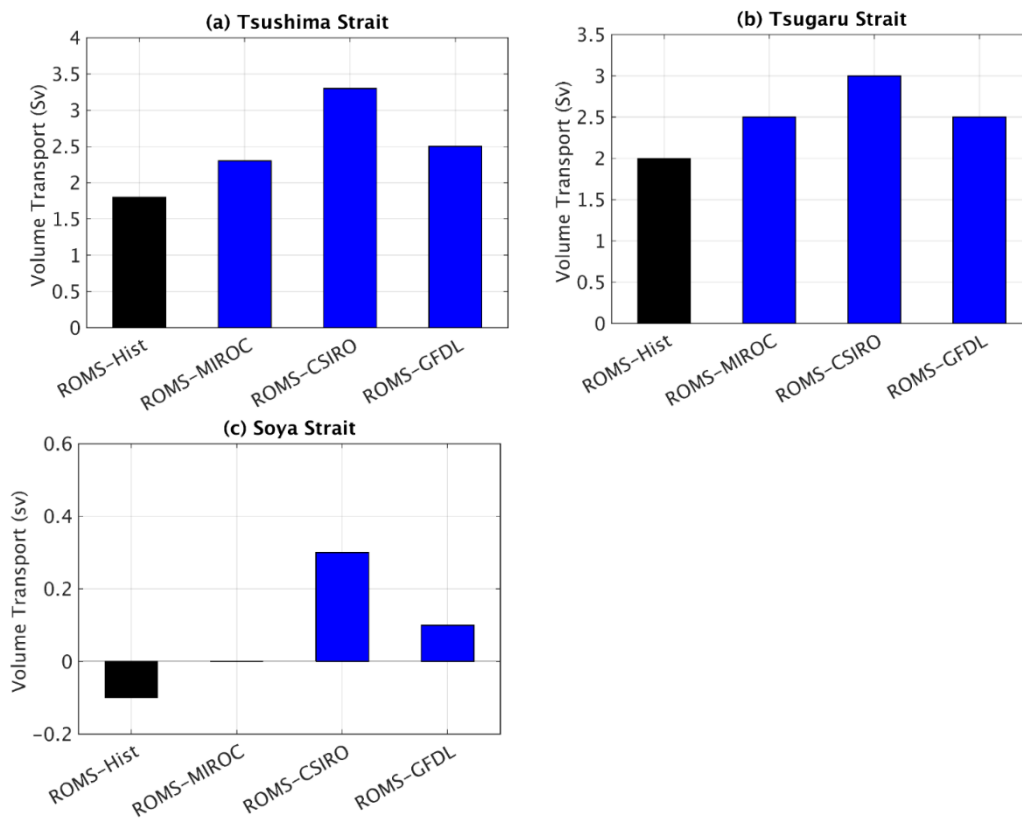


Fig. 20 Time-mean volume transports (in Sv) through (a) Tsushima, (b) Tsugaru, and (c) Soya Strait for 1981–2000 (black) and 2081–2100 (blue) simulated by ROMS downscaling.

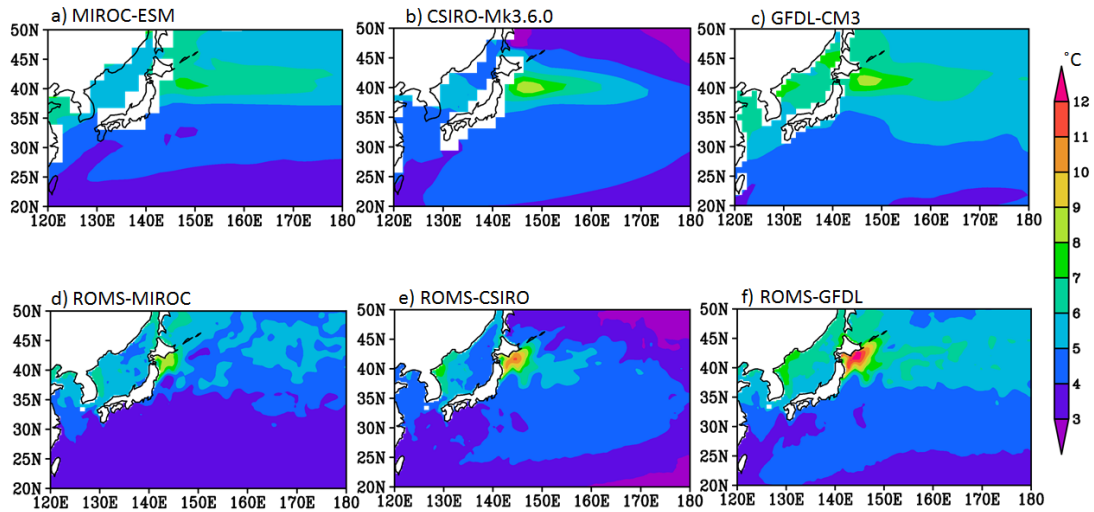


Fig. 21 Projected SST change ($^{\circ}\text{C}$) for 2081–2100 and 1981–2000 in (top) the CMIP5 models and in (bottom) ROMS downscaling simulations for (left) MIROC-ESM, (middle) CSIRO-Mk3.6.0, and (right) GFDL-CM3, respectively.

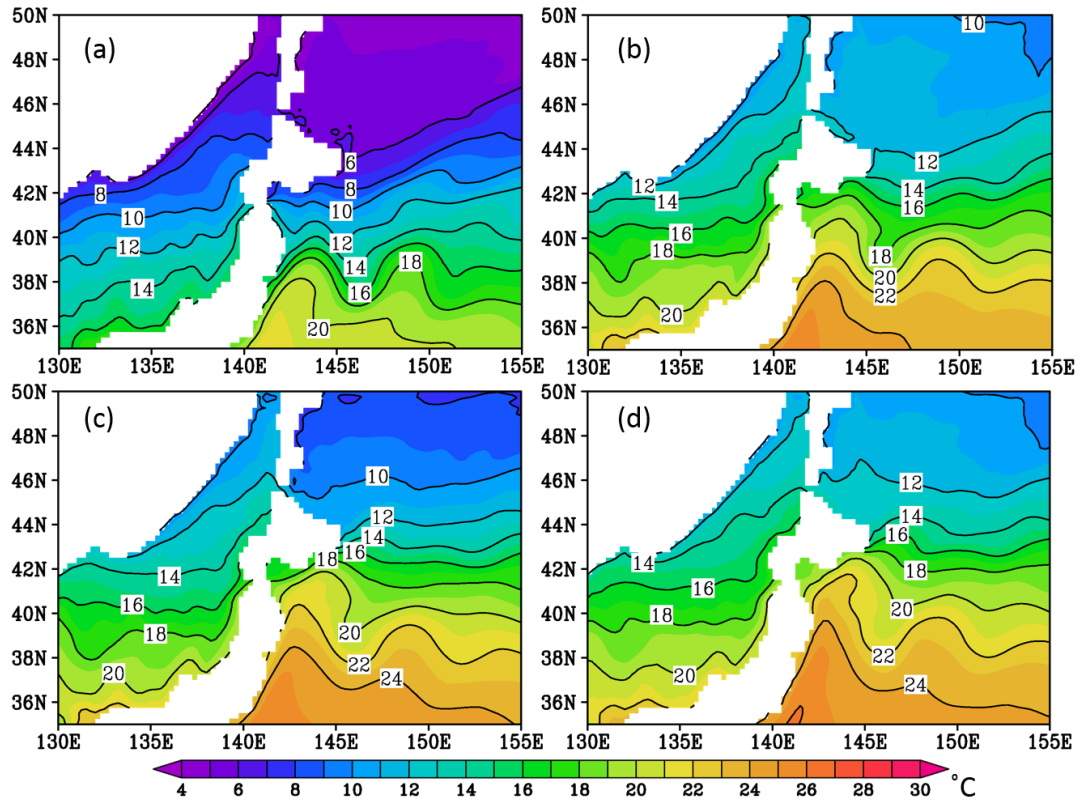


Fig. 22 Time-mean SST (a) in ROMS-Hist during 1981–2000 period, and (b) ROMS-MIROC, (c) ROMS-CSIRO, and (d) ROMS-GFDL during 2081–2100 period.